ADVANCED ENERGY MATERIALS
www.advenergymat.de

Tailored Plum Pudding-Like Co_2P/Sn Encapsulated with Carbon Nanobox Shell as Superior Anode Materials for High-Performance Sodium-Ion Capacitors

Xiaochuan Ren, Zhiguo Ren, Qingwei Li, Wen Wen, Xiaofang Li, Ye Chen, Lei Xie, Liao Zhang, Daming Zhu, Biao Gao, Paul K. Chu, and Kaifu Huo**

Sodium-ion capacitors (SICs) are emerging energy storage devices with high energy, high power, and durable life. Sn is a promising anode material for lithium storage, but the poor conductivity of the a-NaSn phase upon sodaition hinders its implementation in SICs. Herein, a superior Sn-based anode material consisting of plum pudding-like Co_2P/Sn yolk encapsulated with nitrogen-doped carbon nanobox (Co_2P/Sn@NC) for high-performance SICs is reported. The 8–10 nm metallic nanoparticles produced in situ are uniformly dispersed in the amorphous Sn matrix serving as conductive fillers to facilitate electron transfer in spite of the formation of electrically resistive a-NaSn phase during cycling. Meanwhile, the carbon shell buffers the large expansion of active Sn and provides a stable electrode–electrolyte interface. Owing to these merits, the yolk–shell Co_2P/Sn@NC demonstrates a large capacity of 394 mA h g^{-1} at 100 mA g^{-1}, high rate capability of 168 mA h g^{-1} at 5000 mA g^{-1}, and excellent cyclability with 87% capacity retention after 10 000 cycles. By integrating the Co_2P/Sn@NC anode with a peanut shell-derived carbon cathode in the SIC, high energy densities of 112.3 and 43.7 Wh kg^{-1} at power densities of 100 and 10 000 W kg^{-1} are achieved.

X. C. Ren, Z. G. Ren, Dr. Q. W. Li, X. F. Li, Y. Chen, L. Xie, L. Zhang, Prof. K. F. Huo
Wuhan National Laboratory for Optoelectronics (WNLO)
Huazhong University of Science and Technology
Luoyu Road 1037, Wuhan 430074, China
E-mail: kfhuo@hust.edu.cn

Dr. W. Wen, Dr. D. M. Zhu
Shanghai Synchrotron Radiation Facility
Shanghai Advanced Research Institute
Chinese Academy of Sciences
Shanghai 201204, China
E-mail: zhudaming@sinap.ac.cn

Dr. B. Gao
The State Key Laboratory of Refractories and Metallurgy
Institute of Advanced Materials and Nanotechnology
Wuhan University of Science and Technology
Wuhan 430081, China

Dr. B. Gao, Prof. P. K. Chu
Department of Physics and Department of Materials Science and Engineering
City University of Hong Kong
Tat Chee Avenue, Kowloon, Hong Kong 990077, China

The ORCID identification number(s) for the author(s) of this article can be found under https://doi.org/10.1002/aenm.201900091.

DOI: 10.1002/aenm.201900091

1. Introduction

The ever-increasing demand for renewable energy storage and concerns about pollution caused by burning of fossil fuels is spurring rapid development of advanced energy storage technologies.[1] Rechargeable batteries and supercapacitors (SCs) are the two main electrochemical energy storage systems.[2] Although SCs can deliver high power and long lifetime, they suffer from low energy density, and batteries can generally deliver a high energy density but at the expense of low power density and poor long-term cycling stability. To boost the energy density of SCs without compromising the high power or cycle life, hybrid capacitors such as lithium-ion capacitors (LICs), which combine lithium-ion battery-type anodes and capacitor-type cathodes in a Li-salt-containing organic electrolyte, have been proposed.[3,4] Compared to LIBs, sodium-ion capacitors (SICs) are more economical because sodium (Na) is more abundant than Li.[5] However, the design of high-performance anode materials with fast Na-ion reaction kinetics, high capacity, and good cycling is more challenging due to the larger ionic radius of Na^+ (1.02 Å) compared to Li^+ (0.67 Å).[6]

Metallic tin (Sn) has been explored as high capacity anode materials in LIBs due to the high theoretical capacity (997 mA h g^{-1} in the form of $Li_{4.4}Sn$).[7] Nevertheless, the large volume change of Sn during alloying/dealloying causes severe pulverization and an unstable solid electrolyte interphase (SEI) film resulting in quick capacity fading.[8] To overcome these hurdles, yolk–shell Sn@C nanostructures have been designed for LIBs anodes.[9] In the yolk–shell Sn@C structure, the inner void can accommodate Sn expansion whereas the outer carbon shell prevents agglomeration of active Sn and maintains the stability of the SEI films during cycling. Moreover, the carbon shell improves the conductivity throughout the electrode and accelerates the electrochemical kinetics. Therefore, yolk–shell Sn@C nanoboxes have been demonstrated to deliver good Li-ion storage performance in terms of large capacity, high rate capability, and long cycle life. However, the yolk–shell Sn@C nanoparticles are not suitable for efficient Na-ion storage because of the poor conductivity of the in-situ formed

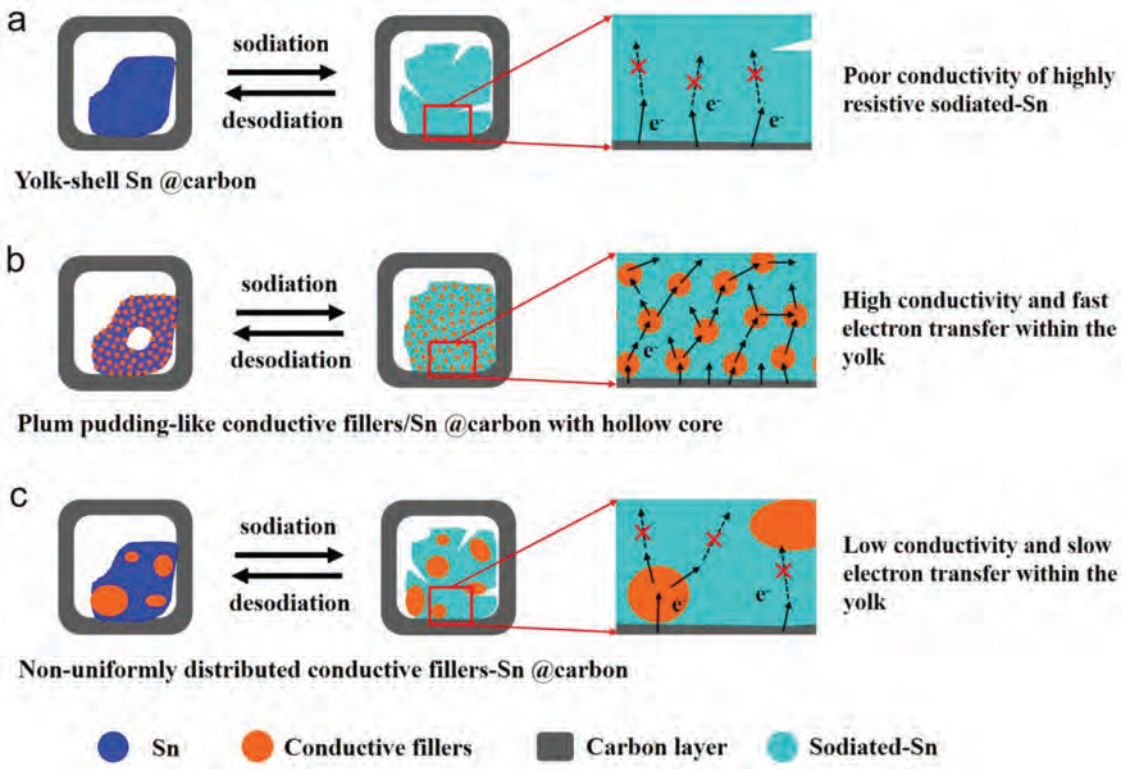

Figure 1. Schematic illustration of the electrochemical process in the three yolk–shell nanobox: a) Yolk–shell Sn@C suffering from the much larger resistance due to electrically resistive a-NaSn during the sodiation process showing poor faradic reaction kinetics; b) Plum pudding-like conductive fillers/Sn@C in which the conductive fillers facilitate electron transfer in the yolk via the field-assisted tunneling effect to maintain the high conductivity during sodiation leading to fast Na-ion storage kinetics and utilization ratio; c) Nonuniformly distributed conductive fillers–Sn causing low conductivity and slow electron transfer in the yolk.

electrically resistive Na-Sn phase during sodiation process that is approximately eight orders of magnitude worse than that of metallic Sn.[10] As schematically shown in **Figure 1**a, the much larger electrical resistivity of Sn during sodiation invariably hampers electron transport in the Sn yolk and compromises the battery, resulting in poor rate capability, low electrochemical utilization, and rapid capacity decay. In this context, if small metallic nanoparticles (NPs) are uniformly embedded in the Sn yolk and then dispersed in the electrically resistive Na-Sn phase to form a plum pudding-like structure during cycling, a high-conductivity can be maintained in the yolk during cycling because the metallic NPs as conductive fillers facilitate electron transfer via the field-assisted tunneling effect (Figure 1b). The plum pudding-like metal NPs/Sn yolk encapsulated with carbon shell is expected to produce fast electron transport and ion diffusion during the sodiating/desodiating process, and the much improved electrochemical performance of Na-ion storage could be achieved. However, owing to the low melting point of Sn (232 °C) and the tendency of melting at a high temperature, the metal NPs/Sn composites always suffer from phase separation and aggregation of conductive NPs and Sn (Figure 1c), resulting in compromised electrical conductivity and Na storage performance. Based on these considerations, the yolk–shell Sn-based nanostructures schematically illustrated in Figure 1b are desirable for efficient Na-ion storage; however, controlled synthesis of metallic NPs/Sn@C nanoboxes in which the plum pudding-like metallic NPs are less than 10 nm and uniformly embedded in Sn on the nanoscale with a suitable filler fraction has not been reported so far.

Herein, we report a novel strategy to controllably synthesize the yolk–shell Co_2P/Sn@ N-doped carbon shell (Co_2P/Sn@NC) consisting of the plum pudding-like Co_2P/Sn yolk and NC shell nanobox as high-power and long cycle-life anode materials in SICs. The Co_2P/Sn@NC nanoboxes are prepared by thermally phosphating polydopamine (PDA) coated hollow $CoSn(OH)_6$ nanocubes. During this process, the 8–10 nm metallic Co_2P in situ produced are homogeneously dispersed in the amorphous Sn matrix to form the plum pudding-like Co_2P/Sn yolk, which is encapsulated with the NC shell nanobox derived from the PDA coating, resulting in the formation of the yolk–shell Co_2P/Sn@NC nanobox. This unique structure has several remarkable features pertaining to efficient Na-ion storage. First, the inner void arising from the hollow core of $CoSn(OH)_6$ and elimination of hydrogen and oxygen can buffer the expansion of Co_2P/Sn without breaking the outer carbon shell during cycling. Second, the 8–10 nm metallic Co_2P NPs are uniformly embedded in the Sn yolk, which can also be converted into metal Co NPs and homogeneously dispersed in the electrically resistive Na-Sn phase during the sodiation process to facilitate electron transfer via the field-assisted tunneling effect during cycling.[11] Therefore, the homogeneous plum pudding-like Co_2P/Sn@NC boasts high conductivity, structural stability,

cyclability, and rate capability during cycling. Additionally, Co_2P also provides capacity for Na-ion storage during cycling. Third, the carbon nanobox shell not only improves the electrical conductivity throughout the electrode and prevents agglomeration of active Sn but also provides stable electrode–electrolyte contact to stabilize the SEI during cycling. Benefiting from these merits and synergetic effects, the Co_2P/Sn@NC electrode exhibits a large capacity of 394 mA h g^{-1} at 100 mA g^{-1}, high rate capability of 168 mA h g^{-1} at 5 A g^{-1}, as well as excellent cyclability with 87% capacity retention after over 10 000 cycles. All the capacities of Co_2P/Sn@NC for Na-ion storage are based on the total mass of Co_2P/Sn@NC, unless otherwise stated. By combining the Co_2P/Sn@NC anode with a peanut shell-derived active carbon cathode, the SIC shows high energy densities of 112.3 Wh kg^{-1} at a power density of 100 W kg^{-1} and 43.7 Wh kg^{-1} at 10 000 W kg^{-1} and excellent cycle stability with 84% capacity retention after 10 000 cycles.

2. Results and Discussion

Figure 2a schematically illustrates the synthesis procedures of the yolk–shell Co_2P/Sn@NC nanobox consisting of the plum pudding-like Sn/Co_2P core encapsulated with a NC shell. The $CoSn(OH)_6$ nanocubes as the precursor are synthesized hydrothermally,[12] and dopamine is used as the precursor of carbon shell, which can self-polymerize into PDA coating immobilized on $CoSn(OH)_6$ with robust adhesion.[9a] The plum pudding-like Co_2P/Sn@NC nanobox is prepared by thermally phosphating PDA-coated $CoSn(OH)_6$ nanocube at 300 °C with NaH_2PO_2 as phosphorus source and then further annealing at 400 °C under H_2/Ar. During this process, the $CoSn(OH)_6$ core is reduced to produce the plum pudding-like Co_2P/Sn in situ and at the same time, the PDA coating is carbonized into the NC shell yielding the yolk–shell Co_2P/Sn@NC nanobox. The field-emission scanning electron microscopy (FESEM, Figure S1, Supporting Information) and transmission electron microscopy (TEM) images (Figure 2b) reveal that the as-prepared $CoSn(OH)_6$ possess a cubic structure with high uniformity and the size of $CoSn(OH)_6$ is 200–250 nm. The TEM images in Figure 2b confirm the well-defined hollow core structure of the $CoSn(OH)_6$ nanocubes. The corresponding X-ray diffraction (XRD) pattern is indexed to the standard $CoSn(OH)_6$ (JCPDS No. 13-0356, Figure S2, Supporting Information).[12] The TEM images (Figure 2c and Figure S3a, Supporting Information) of the core–shell $CoSn(OH)_6$@PDA reveal that the PDA coating covers the $CoSn(OH)_6$ nanocubes and has a thickness of 18 nm. After the thermal reaction, the product maintains the cubic morphology (Figure 2d,e) and more void appears due to the elimination of oxygen and hydrogen (Figure 2d). The core is confined inside the NC shell with inner void forming the yolk–shell nanobox structure. The high-resolution TEM (HRTEM) image of the yolk (Figure 2f) shows that the 8–10 nm crystalline Co_2P NPs are uniformly dispersed in the amorphous Sn matrix forming a plum pudding-like structure, and the thickness of outer NC shell is about 14 nm (Figure S3b, Supporting Information). The presence of N in the NC shell is confirmed by X-ray photoelectron spectroscopy (XPS) (Figure S3c,d, Supporting Information) and X-ray energy-dispersive spectrometer (EDS) results (Figure S4, Supporting Information). The N content is about 2.5 wt%. The N 1s XPS spectrum can be fitted into three peaks located at 398.5, 400.1, and 398.5 eV corresponding to the binding energy of pyridinic N, pyrrolic N, and graphitic N, respectively.[13b] The XPS spectrum of C 1s can be deconvoluted into three peaks. The main peak at 284.6 eV is assigned to the graphite-like C, and the small peaks at 285.5 and 286.7 eV are attributed to the C—O and C—N—C bonds, respectively.[13b] The two Raman peaks at 1347 and 1585 cm^{-1} are assigned to the vibration modes of disordered graphite (D band) and E_{2g} of crystalline graphite (G band), and the large I_D/I_G ratio (1.15) reflects the low graphitic degree of the carbon coating (Figure S3e, Supporting Information). The corresponding XRD pattern confirms the Co_2P phase (JCPDS No. 32-0306) and no XRD patterns related to Sn and C are observed due to the amorphous feature. The EDS spectrum (Figure S4, Supporting Information) shows that the atomic ratio of Co and Sn is nearly 1:1, and the Sn 3d fine XPS spectrum (Figure S5, Supporting Information) confirms that Sn is metallic Sn with zero valence. The uniform distribution of Co_2P NPs in the Sn matrix is corroborated by high-angle annular dark-field scanning TEM (HAADF-STEM) and elemental mapping (Figure 2h,i and Figure S6, Supporting Information). The overlapping elemental distributions of Co, P, Sn, C, and N suggest a uniform Co_2P/Sn yolk@NC-box-shell structure. The carbon concentration in the Co_2P/Sn@NC is determined to be 23.4 wt% by thermogravimetric analysis (TGA) as shown in Figure S7 (Supporting Information). The yolk–shell Co_2P/Sn@NC nanobox is similar to the nanostructure schematically depicted in Figure 1b and favorable to Na-ion storage. For comparison, Co_2P/Sn without the NC shell is also prepared by thermally phosphating $CoSn(OH)_6$ without the PDA coating under the same experimental conditions. SEM and TEM images reveal that Co_2P/Sn retains the cubic morphology (Figure S8a, Supporting Information) and plum pudding-like Co_2P/Sn structure (Figure 2f and Figure S8b–d, Supporting Information). However, when the thermal treatment temperature is increased to 500 °C, the cubic structure is broken and the two separated phases of Sn and Co_2P can be identified (Figure S9, Supporting Information). Although the cubic morphology could be retained with the NC shell via further thermal annealing under Ar/H_2 at 500 °C, the EDS mapping discloses nonuniform distributions of Sn and Co_2P particles in the yolk (Figure S10, Supporting Information). XRD result (Figure S11, Supporting Information) reveals that the amorphous Sn is converted into the crystalline phase Sn (JCPDS No. 04-0673), resulting in the formation of an inhomogeneous mixture of crystalline Sn and Co_2P particles. Such nanobox is denoted as Co_2P-Sn@NC, which has a similar nanostructure schematically shown in Figure 1c.

Our results confirm that the plum pudding-like Co_2P/Sn@NC and nonuniformly distributed Co_2P-Sn@NC can be controllably synthesized by changing the second-step annealing temperature under H_2/Ar after thermal phosphating of the $CoSn(OH)_6$@PDA at 300 °C. To investigate the formation mechanism, the samples of the thermally phosphated $CoSn(OH)_6$@PDA at 300 °C are analyzed. XPS and XRD (Figures S5 and S12, Supporting Information) reveal that the thermally phosphating product is composed of crystalline Co_2P and amorphous SnO_x, which are encapsulated by C shell.

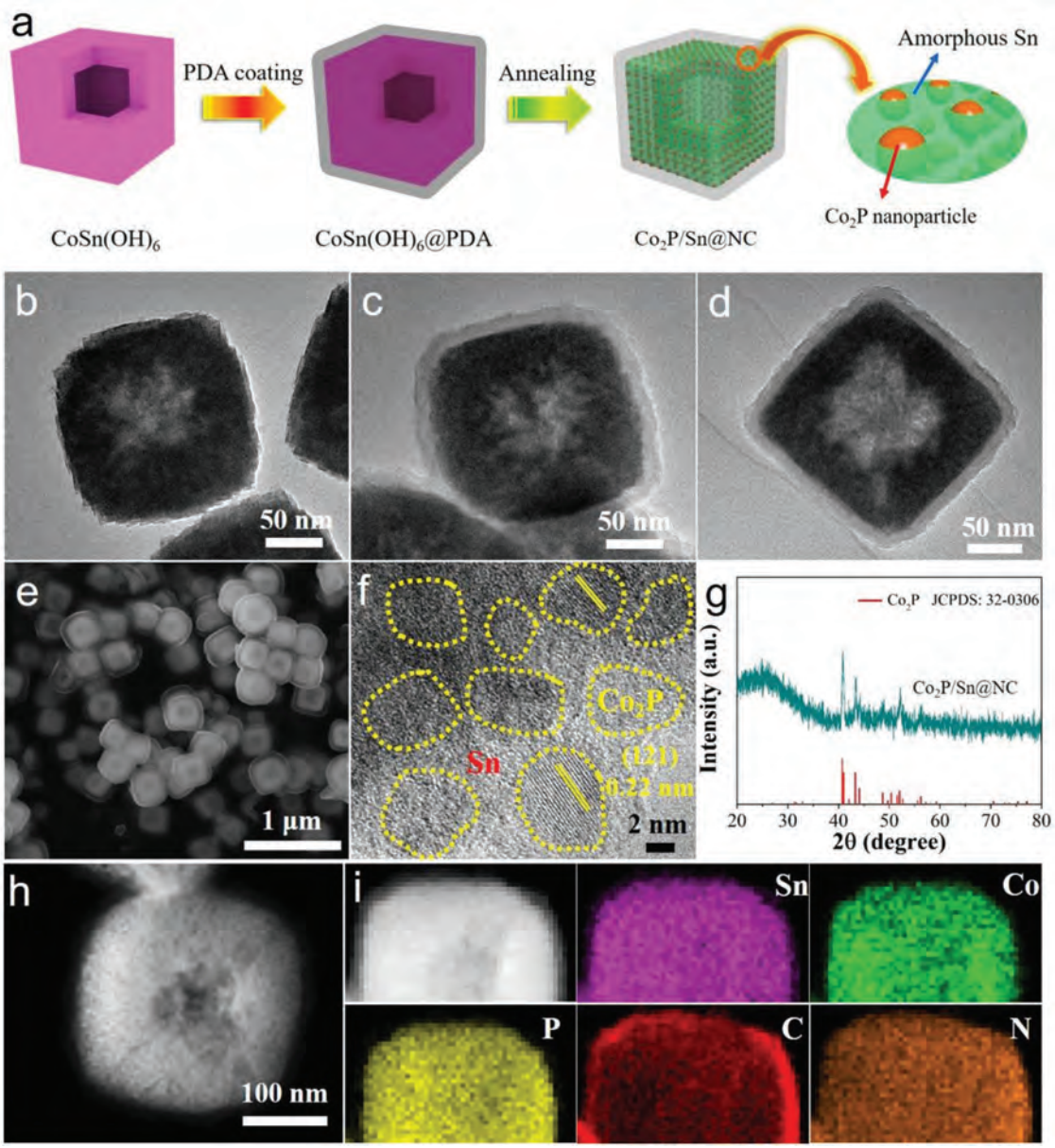

Figure 2. a) Schematic illustration of the preparation of the yolk–shell Co_2P/Sn@NC nanobox. b–d) TEM images of $CoSn(OH)_6$, $CoSn(OH)_6$@PDA, and Co_2P/Sn@NC nanobox. e) FESEM image of Co_2P/Sn@NC. f) HRTEM image of the Co_2P/Sn. g) XRD pattern and h) HAADF-STEM images and corresponding elemental maps of the Co_2P/Sn@NC nanobox.

During thermal annealing under H_2/Ar at 400 °C, the amorphous SnO_x is reduced to form liquid Sn because of the low melting point (232 °C). Due to the similar density of liquid Sn and Co_2P (≈7 g cm^{-3}), the Co_2P NPs could homogeneously disperse in the molten Sn. After cooling, Sn solidifies to produce the plum pudding-like Co_2P/Sn, which is encapsulated with the NC shell forming the Co_2P/Sn@NC nanobox. The uniform distribution of Co_2P NPs in Sn nanomatrix causes a restricted spatial dimension and sufficient internal strain to prevent crystallization of Sn;[14] therefore, the Sn in Co_2P/Sn@NC is amorphous, which is confirmed by TEM and XRD results (Figure 2f,g). However, if the annealing temperature is increased to 500 °C, SnO_x is quickly reduced to form liquid Sn droplets, which are aggregated and pooled together resulting in the formation of large crystalline Sn and Co_2P particles. As a result, the Sn phase with a high intensity in the XRD from the Co_2P-Sn@NC sample is observed.

The electrochemical performances of the Co_2P/Sn@NC and Co_2P-Sn@NC electrodes are evaluated using half cells with the Na foil as the counter electrode. **Figure 3**a shows the first four cyclic voltammetry (CV) curves of the Co_2P/Sn@NC electrode at a scanning rate of 0.2 mV s^{-1} between 0.001 and 3.0 V. In the first cycle, the broad reduction peak at 0.63 V in the discharge process can be assigned to the overlying peaks composed of the formation of a SEI film and reduction of Co_2P to Co metal and Na_3P. The sloping line below 0.5 V in the first

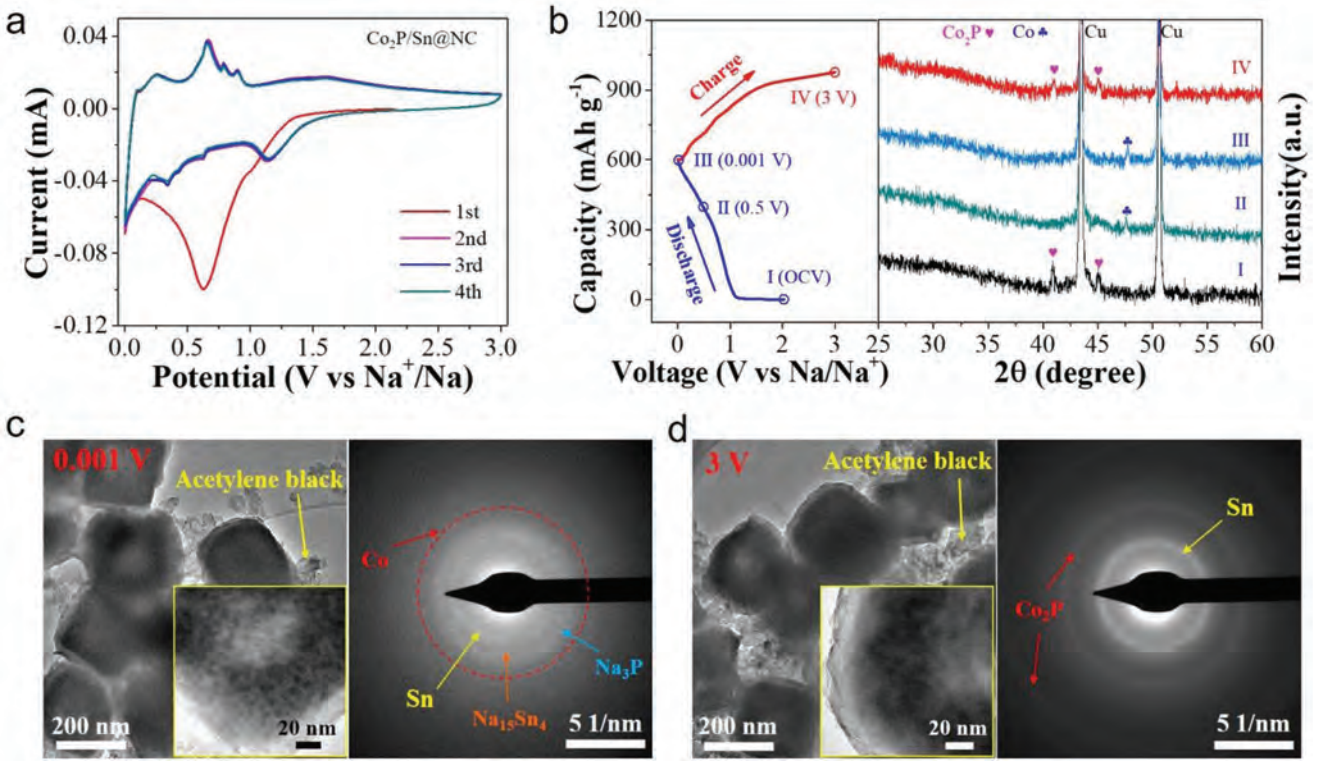

Figure 3. a) CV curves of the Co_2P/Sn@NC electrode at a scanning rate of 0.2 mV s^{-1}. b) Charge–discharge profiles and corresponding ex situ XRD patterns of the Co_2P/Sn@NC electrode during the first cycle. Ex situ TEM images and SAED patterns of Co_2P/Sn@NC at the c) discharged states of 0.001 V and d) charged state of 3 V.

sodiation process can be ascribed to the gradual sodiation reactions of Sn to produce the final amorphous $Na_{15}Sn_4$.[15] During the anodic scan, the broad anodic peaks below 1.0 V stem from the stepwise desodiation reaction of $Na_{15}Sn_4$ to Na_xSn intermediates and final Sn.[13] The anodic broad peak at 1.5 V arises from the reverse reaction of Co metal to form Co_2P. The sodiation and desolation process of Co_2P/Sn@NC in the CV curve is supported by the ex situ XRD patterns in Figure 3b. After the first CV circle, the curves overlap demonstrating the excellent reversibility of the Co_2P/Sn@NC for efficient Na^+ storage. TEM images (Figure 3c,d) disclose that the microstructure and cubic morphology of Co_2P/Sn@NC could be well-retained during cycles. Ex situ selected area electron diffraction (SAED), which could identify small and poor crystallinity phase of Na_xSn, is performed to further confirm the reversible reaction of Sn and Co_2P during cycling. The ex situ SAED pattern at discharging 0.001 V (Figure 3c) displays a few obscure and broad lattice fringes with *d*-spacings of ≈0.29, 0.26, and 0.24 nm, corresponding to amorphous Sn (JCPDS No. 04-0673), $Na_{15}Sn_4$ (JCPDS No. 31-1327), and Na_3P (JCPDS No. 74-1164) phases, respectively. The lattice fringes with a *d*-spacing of 0.19 nm can be indexed to crystalline Co (101) (JCPDS No. 05-0727). After charging to 3 V, the SAED pattern (Figure 3d) can be indexed to a mixture of Sn and Co_2P further confirming the excellent reversibility of the Co_2P/Sn@NC anode.

The electrochemical performances of Co_2P/Sn@NC and Co_2P-Sn@NC are compared to assess the structural advantage of Co_2P/Sn@NC for Na storage. The CV curves of Co_2P/Sn@NC and Co_2P-Sn@NC electrodes during second cycle are depicted in **Figure 4**a. The cathodic peaks of a, b, c, and d are assigned to the gradually alloying reaction of Sn to $NaSn_5$, a-NaSn, Na_9Sn_4, and $Na_{15}Sn_4$, respectively.[13a] The anodic peaks of e, f, g, and h are attributed to the corresponding reverse reactions from $Na_{15}Sn_4$ to Na_9Sn_4, a-NaSn, $NaSn_5$, and finally Sn.[13a] Compared to Co_2P-Sn@NC electrode, the Co_2P/Sn@NC exhibits much stronger cathodic peaks at 0.34 V and anodic peaks at 0.66 and 0.79 V, which are related to the sodiation reaction of a-NaSn phase to Na_9Sn_4 and desodiation of Na_9Sn_4 to a-NaSn and then to $NaSn_5$, respectively. It has been shown that the resistivity of the Sn anode can increase by about eight orders of magnitude when metallic Sn is converted to the sodiated-Sn phase during the in situ sodiation process due to the presence of resistive Zintl ions (Sn_4^{4-}, covalently bonded Sn clusters) in a-NaSn and the stress of a-NaSn.[10] The considerably larger resistance of a-NaSn hinders electron transfer in the sodiated Sn (as schematically depicted in Figure 1a) giving rise to a low capacity and poor rate performance. Compared to Co_2P-Sn@NC, Co_2P/Sn@NC has improved overall conductivity due to the homogeneous distribution of metallic Co_2P NPs in the Sn matrix, the Sn and a-NaSn phase thus exhibiting higher electrochemical utilization, thereby resulting in stronger anodic and cathodic peaks in CV and improved Na-storage for the Co_2P/Sn@NC electrode. To further investigate the different electrochemical properties of the Co_2P/Sn@NC and Co_2P-Sn@NC electrodes, electrochemical impedance spectroscopy (EIS) is performed at different charging/discharging

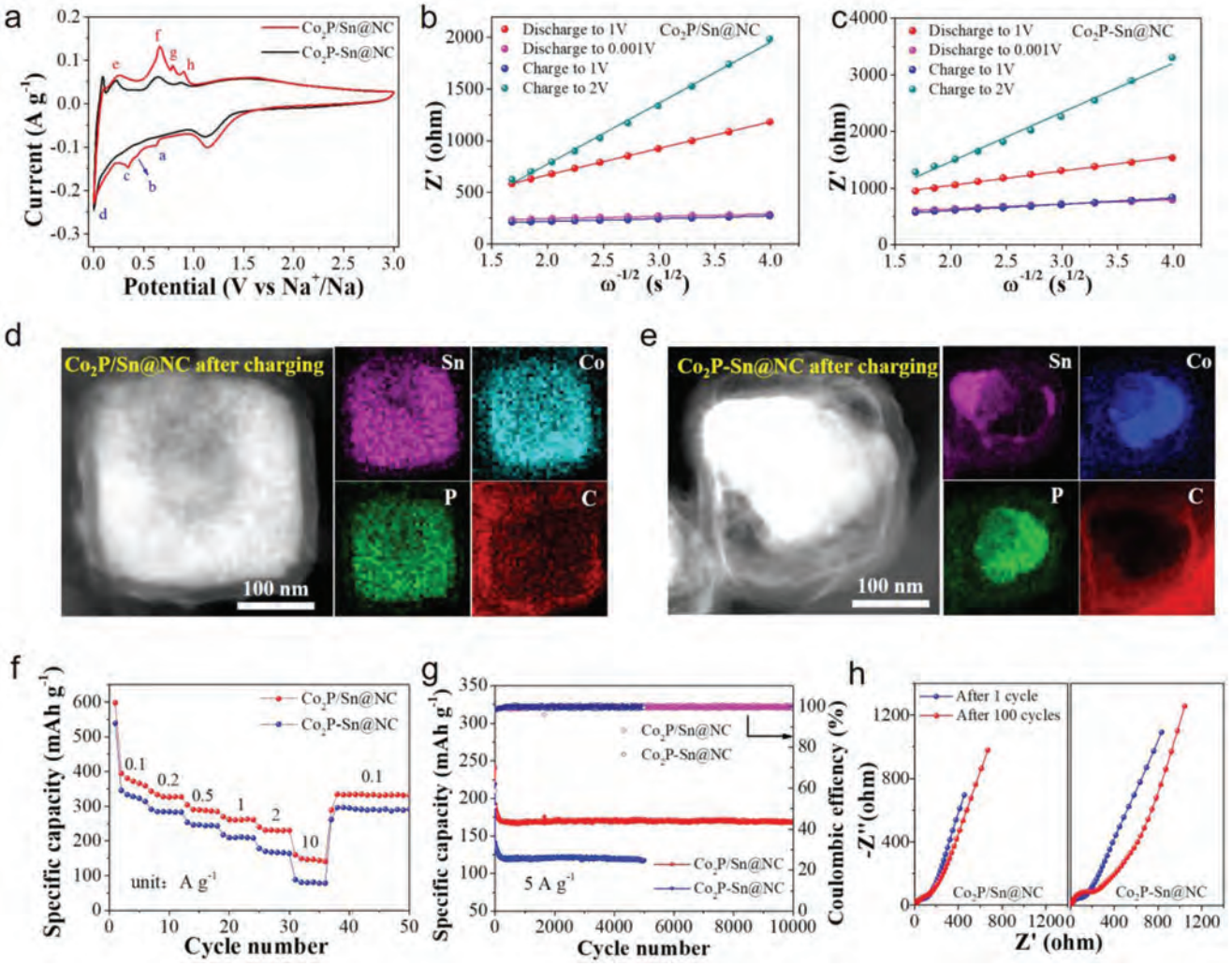

Figure 4. a) Comparison of the CV curves between the Co_2P/Sn@NC and Co_2P-Sn@NC electrodes at a scanning rate of 0.2 mV s^{-1} during second cycle. b,c) The plots of the real part of the impedance (Z') as a function of the inverse square root of the angular frequency ($\omega^{-1/2}$) in the Warburg region in the first cycle for Co_2P/Sn@NC and Co_2P-Sn@NC. d,e) The HAADF-STEM and corresponding elemental maps of Co_2P/Sn@NC and Co_2P-Sn@NC charged at 3 V. f) Rate capability and g) cycling performance of the Co_2P/Sn@NC and Co_2P-Sn@NC electrodes. h) EIS results of Co_2P/Sn@NC and Co_2P-Sn@NC after the 1st and 100th cycle.

stages (Figure S13, Supporting Information). The two compressed semicircles observed at high and medium frequencies are related to the resistance of the SEI film (R_{SEI}) and the charge transfer resistance (R_{ct}) of the electrodes, respectively.[16] The Co_2P/Sn@NC electrode exhibits much lower R_{ct} and R_s (Ohmic resistance) values than Co_2P-Sn@NC during the whole charging/discharging process (Figure S13, Supporting Information) due to the internal conductive networks enabled by the homogeneous plum pudding-like Co_2P/Sn yolk. The Na^+ diffusion coefficient (D_{Na}) is calculated to further explore the advantage of the special structure of Co_2P/a-Sn@NC for Na^+ storage. D_{Na} can be calculated from the plots in the low-frequency region of the EIS curve based on the following equations, $D_{Na} = R^2T^2/2n^4F^4\sigma_w{}^2A^2C^2$ and $Z = R1 + \sigma_w\omega^{-1/2}$. In these two equations, R is the gas constant, T is the absolute temperature, n is the number of electrons per molecule during oxidization, F is Faraday's constant, A is the surface area of the electrode, C is the Na^+ concentration in the electrode material, Z is the real impedance (Z'), $R1$ is the resistance, σ_w is the Warburg coefficient, and ω is the angle frequency.[17] σ_w can be obtained from the slope of Z versus $\omega^{-1/2}$ in the Warburg region as shown in Figure 4b,c for the Co_2P/Sn@NC and Co_2P-Sn@NC electrodes, respectively. The σ_w and D_{Na} values of the Co_2P/Sn@NC and Co_2P-Sn@NC electrodes at various potentials are presented in Table S1 (Supporting Information). The calculated D_{Na} values of the Co_2P/Sn@NC electrode are much larger than those of the Co_2P-Sn@NC electrode at the various sodiation/desodiation stages. Specifically, the D_{Na} values of Co_2P/Sn@NC are nearly 12 and 18 times higher than those of Co_2P-Sn@NC at the discharging stage of 0.001 V and charging stage of 1 V, respectively. The enhanced Na^+ diffusion coefficient of Co_2P/Sn@NC can be attributed to the homogeneous plum pudding-like Co_2P/Sn yolk, which can resist the large resistance amplification of Sn and facilitate fast ions/electrons diffusion. The

morphological evolution of Co_2P/Sn@NC and Co_2P-Sn@NC during the cycling process is observed by HAADF-STEM and elemental mapping at 0.001 and 3.0 V. After charging and discharging, Co_2P/Sn@NC maintains the pristine plum pudding-like Co_2P/Sn@NC morphology without obvious change, and Co, Sn, P, C, and N uniformly distribute in the yolk (Figure 4d and Figure S14, Supporting Information). However, aggregation and nonuniformly distributed Sn, Co, and P elements are observed in the yolk (Figure 4e) confirming phase segregation of Sn and Co_2P in Co_2P-Sn@NC after charging to 3 V. The plum pudding-like Co_2P/Sn@NC facilitates fast ion/electron diffusion and maintains structural stability during cycling, consequently enhances the electrochemical Na-ion storage properties in comparison with the nonuniformly distributed Co_2P-Sn@NC.

The rate and cycle characteristics of the Co_2P/Sn@NC and Co_2P-Sn@NC electrodes are measured in the range of 0.001–3 V. All the capacities are based on the total mass of Co_2P/Sn@NC or Co_2P-Sn@NC. As shown in Figure 4f, the Co_2P/Sn@NC electrode has enhanced rate capability. As the current density is increased from 0.1 to 0.2, 0.5, 1, 2, and 10 A g^{-1}, the reversible capacity decreases from 394 to 336, 291, 264, 233, and 147 mA h g^{-1}, respectively. When the current density is returned to 0.1 A g^{-1}, a reversible capacity of 336 mA h g^{-1} is recovered, suggesting high reversibility. In contrast, the Co_2P-Sn@NC electrode shows lower capacity and poor rate characteristics, especially at high current density due to the low reactivity of Sn and poor conductivity during sodiation/desodiation processes caused by the inhomogeneously distributed conductive Co_2P. The cycling performance of the Co_2P/Sn@NC and Co_2P-Sn@NC electrodes is presented in Figure 4g. The Co_2P/Sn@NC delivers a high capacity of 168 mA h g^{-1} after 10 000 cycles at 5 A g^{-1} with a negligible capacity fading rate of 0.0012% per cycle and nearly 100% of coulombic efficiency (CE). However, the Co_2P-Sn@NC electrode has a low specific capacity although it also shows good capacity retention. Table S2 (Supporting Information) lists the Na-ion storage properties of Sn or Sn alloy reported in the literatures. If we calculate the capacity of Co_2P/Sn@NC based on the mass loading of Sn, the Co_2P/Sn@NC has better Na-ion storage properties in terms of the capacity, rate capability, and cycle stability. EIS is also performed on the Co_2P/Sn@NC and Co_2P-Sn@NC electrodes after the 100th cycle. As shown in Figure 3h, the Co_2P/Sn@NC electrode has similar R_{ct} values after the 1st and 100th cycles but R_{ct} of Co_2P-Sn@NC increases after the 100th cycle suggesting the better cycle reversibility of Co_2P/Sn@NC electrode. As schematically shown in Figure 1b, the homogeneous plum pudding-like Co_2P/Sn@NC can resist large resistance amplification of Sn during sodiation and facilitate electron transfer, thereby resulting in enhanced electrochemical Na-ion storage compared to the nonuniformly distributed Co_2P-Sn@NC. To further reveal the role of NPs as conductive fillers in Sn anodes, we also prepared the yolk–shell Sn@NC nanobox without metallic Co_2P NPs. The synthesis method is similar to the previous report,[9a] and dopamine is employed as the precursor of the carbon shell as the case in the synthesis of Co_2P/Sn@NC. The synthesis details, morphology, structure, and composition characterizations of Sn@C box are provided in Figure S15 (Supporting Information). TEM observation reveals the yolk–shell Sn@C cubic nanobox with the size of 150–200 nm and the carbon shell of 17 nm, which are confirmed by the EDS mappings (Figure S15a,b, Supporting Information). The XRD pattern in Figure S15c (Supporting Information) is indexed to the tetragonal Sn (JCPDS No. 04-0673), and the carbon shell is amorphous in accordance with the HRTEM results. The carbon content in Sn@C nanobox is about 23.4% based on TGA (Figure S15d, Supporting Information). The cycling performances of the Sn@C and Co_2P/Sn@NC electrodes are presented in Figure S16a (Supporting Information). The Sn@C exhibits a capacity of 31 mA h g^{-1} at 5 A g^{-1} after 500 cycles, which is much lower than that of Co_2P/Sn@NC. Figure S16b (Supporting Information) depicts the rate performances of Sn@C and Co_2P/Sn@NC electrodes at different current densities. Although the Sn@C has higher capacity at 0.1 A g^{-1} compared to Co_2P/Sn@NC due to the higher Sn content, the Co_2P/Sn@NC delivers much higher capacities at the higher current density, indicating the higher electrochemical utilization of Sn in Co_2P/Sn@NC due to the enhanced conductivity during cycling. The homogeneous plum pudding-like Co_2P/Sn@NC can resist large resistance amplification of Sn to electrically resistive a-NaSn and facilitate electron transfer; therefore, Co_2P/Sn@NC exhibits superior Na-ion storage properties compared with Co_2P-Sn@NC and Sn@C electrodes.

To evaluate the commercial potential of Co_2P/Sn@NC, a SIC is assembled by integrating the Co_2P/Sn@NC anode with the peanut shell derived active carbon (PAC) cathode (**Figure 5**a). The electrolyte was composed of 1 M $NaClO_4$ in a mixture of ethylene carbonate (EC), diethylene carbonate (DEC) with 5% fluoroethylene carbonate (FEC) as an additive. The electrochemical properties of the PAC electrode are determined in a half-cell in the potential range of 2.0–4.2 V (vs Na/Na^+) before constructing the SIC (Figure S17, Supporting Information). Figure S17a (Supporting Information) shows the galvanostatic charge/discharge (GCD) profiles of the PAC electrode revealing a linear shape, indicating that the PAC electrode operates at an ideal electrochemical double-layer capacitance. The rate performance of the PAC is shown in Figure S17b (Supporting Information). The PAC cathode has large specific capacities of 91 mA h g^{-1} at 0.1 A g^{-1} and 45 mA h g^{-1} at 10 A g^{-1}. In addition, the PAC cathode delivers excellent cycling performance with 76% retention after 3300 cycles at 1 A g^{-1} (Figure S17c, Supporting Information).

Considering that the majority of the capacity of Co_2P/Sn@NC is contributed in the voltage range of 2–0.01 V (vs Na/Na^+) for the anode and the potential range of the PAC electrode is 2–4.2 V (vs Na/Na^+), the operating voltage range of the SIC is set in the range of 0–4 V to avoid the risk of electrolyte decomposition. As shown in Figure S18 (Supporting Information), the optimal mass ratio between the anode and cathode materials is determined to be 1:3.5 based on the capacity balance to achieve highest energy and power density. Figure 5b shows the GCD profiles of the SIC at current densities between 0.2 and 2 A g^{-1}. During the charging process, Na^+ reacts rapidly with the Co_2P/Sn@NC anode and ClO_4^- adsorbs on the surface of the PAC cathode. Discharging is the reverse process of charging. The cycle performance of the Co_2P/a-Sn@NC//PAC device is investigated at a current density of 2 A g^{-1} (Figure 5c). The SIC device shows excellent capacity retention of ≈84% after 10 000 cycles with a coulombic efficiency of ≈100%. Figure 5d

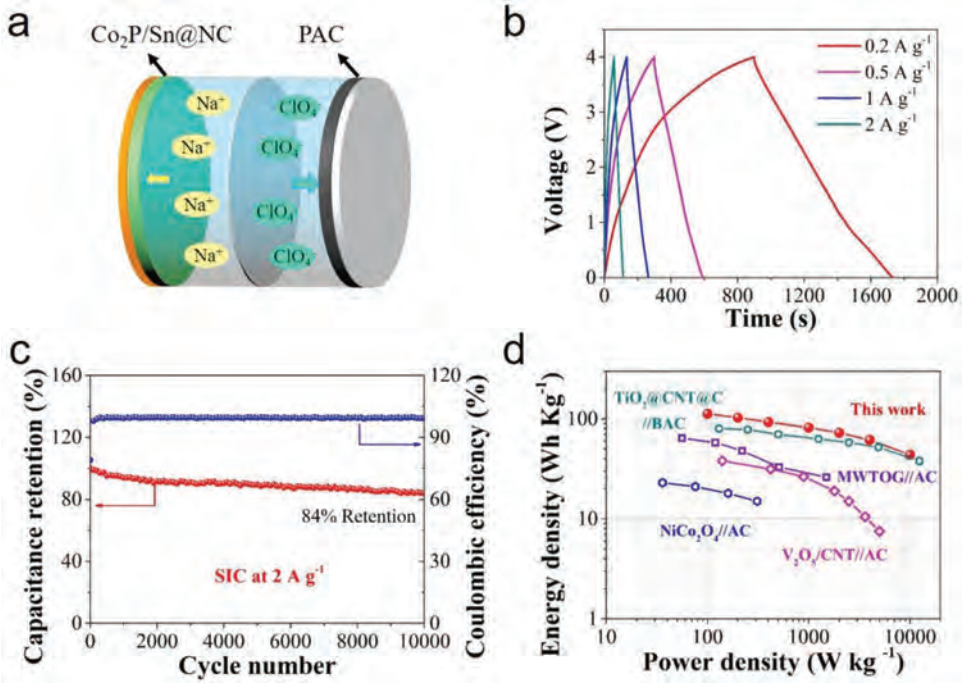

Figure 5. Electrochemical performance of the assembled Co_2P/Sn@NC//PAC SIC device: a) Schematic of the coin cell SIC; b) Galvanostatic charging/discharging profiles of the SIC in the range of 0–4 V at different current densities; c) Cycling stability of the SIC device at a current density of 2 A g^{-1}; d) Ragone plots of the Co_2P/Sn@NC//PAC device compared to the SIC devices in the literature. The energy and power densities are calculated based on the total mass of the cathode and anode materials.

presents the Ragone plot showing the trade-off between the energy and power densities in the assembled SIC. The SIC delivers a high energy density of 112.3 Wh kg^{-1} at a power density of 100 W kg^{-1} based on the total mass of both the anode and cathode electrodes. At a high power density of 10 000 W kg^{-1}, it still delivers a high energy density of 43.7 Wh kg^{-1}. The Ragone plots of other state-of-the-art SICs such as TiO_2@CNT@C//BAC,[6a] MWTOG//AC,[18] $NiCo_2O_4$//AC,[19] and V_2O_5/CNT//AC devices[20] are listed in Figure 5d, and the Co_2P/a-Sn@NC//PAC device with promising energy-power delivery outperforms most of these reported SICs.

3. Conclusion

Yolk-like nanoboxes consisting of the plum pudding-like Co_2P/Sn yolk and NC shell are designed and fabricated controllably as superior anode materials for SICs. Owing to the homogeneous distribution of metallic NPs in the Sn matrix, the Co_2P/Sn@NC maintains the high conductivity to facilitate electron transfer during cycling via the internal conductive network of plum pudding-like metal NPs in spite of the formation of electrically resistive a-NaSn phase during sodiation process. In combination with the NC nanobox shell, the Co_2P/Sn@NC composite exhibits a large capacity and fast electrochemical kinetics. Electrochemical measurements reveal that the Co_2P/Sn@NC anode has a high specific capacity of 394 mA h g^{-1} at 100 mA g^{-1} and 87% capacity retention after 10 000 cycles at 5 A g^{-1}. The high-performance SIC assembled with the Co_2P/Sn@NC anode and peanut shell-derived active carbon cathode exhibits high energy densities of 112.3 Wh kg^{-1} at a power density of 100 W kg^{-1} and 43.7 Wh kg^{-1} at 10 000 W kg^{-1} as well as excellent cycle stability with 84% capacity retention after 10 000 cycles. The results provide insights into the design of electrode materials with high energy and power densities for next-generation SICs.

4. Experimental Section

Synthesis of Yolk–Shell Co_2P/Sn@NC, Sn@NC, and Co_2P-Sn@NC Nanobox: The $CoSn(OH)_6$ nanocubes were synthesized with a large yield by a modified method.[12] Briefly, 15 mL of ethanol containing 3 mmol $SnCl_4$ was added to 105 mL of an aqueous solution containing 3 mmol $CoCl_2$ and 3 mmol sodium citrate under stirring. 15 mL of 2 M NaOH were added dropwise to the above solution at room temperature. After stirring for 1 h, 60 mL of 8 M NaOH was added to the solution and stirred for 15 min. The pink precipitate was harvested by centrifugation and dried in an oven at 60 °C overnight. To prepare the yolk–shell $CoSn(OH)_6$@PDA, 100 mg of the $CoSn(OH)_6$ nanocubes were dispersed in a solution containing 50 mL of deionized water and 50 mL of ethanol. Tris(hydroxymethyl)aminomethane (121 mg) and 50 mg of dopamine hydrochloride were sequentially added and stirred for 12 h at room temperature in air. After centrifugation, washing, and drying, $CoSn(OH)_6$@PDA was obtained. To prepare the yolk–shell Co_2P/Sn@NC nanoboxes, $CoSn(OH)_6$@PDA was thermally treated at 300 °C with NaH_2PO_2 under Ar and further annealed at 400 °C under H_2/Ar. To prepare the Co_2P-Sn@NC nanoboxes, the temperature was raised to 500 °C and segregation of Co_2P and Sn produced large nanoparticles Co_2P and Sn (denoted as Co_2P-Sn@NC nanobox).

The yolk–shell Sn@C nanoboxes were synthesized according to the method in the previous report.[9a] Briefly, 10 mmol of zinc sulfate heptahydrate ($ZnSO_4 \cdot 7H_2O$) and sodium stannate solution

($Na_2SnO_3 \cdot 4H_2O$) was dissolved in 100 and 20 mL deionized water, respectively. Then the two solutions were mixed and vigorously stirred at 60 °C for 4 h. The white precipitates were obtained by centrifugation, washing, and then drying at 80 °C for 5 h. To prepare the yolk–shell Sn@C, 200 mg of as-prepared white powders were dispersed in a solution containing 100 mL of deionized water and 100 mL of ethanol. Tris(hydroxymethyl)aminomethane (242 mg) and 100 mg of dopamine hydrochloride were sequentially added and stirred for 12 h at room temperature. The as-obtained black powers were thermally treated at 650 °C under H_2/N_2 to produce yolk–shell Sn@C nanobox.

Materials Characterization: The morphology, structure, and composition of the samples were studied by XRD (Philips X'Pert Pro with Cu Kα radiation, λ = 1.5418 Å), Raman scattering (HR RamLab), XPS (ESCALB MK-II), FESEM (FEI Nano-SEM 450), and HRTEM (FEI Titan 60-300 Cs). The carbon concentration in Co_2P/Sn@NC was determined by TGA (NETZSCH) in air using a heating rate of 5 °C min^{-1}.

Electrochemical Tests: The electrochemical properties of Co_2P/Sn@NC were evaluated using coin cells (CR2025) with pure Na as the counter electrode. The Co_2P/Sn@NC electrode was prepared by mixing 70 wt% of the active materials, 10 wt% of carboxylmethyl cellulose (CMC), and 20 wt% of acetylene black in deionized water. The slurry was spread on a copper foil and vacuum dried at 80 °C for 6 h. The electrode was punched into disks with a loading of ≈1 mg cm^{-2}. The cell assembly was carried out in an argon-filled glovebox with a separator of glass fiber filter (Whatman GF/C). The electrolyte was composed of 1 M $NaClO_4$ in a mixture of EC, DEC, and 5% FEC. Galvanostatic charging/discharging tests were conducted using the MTI automatic battery cyclers in the potential range between 0.001 and 3.0 V, and CV was performed on the CHI 760D electrochemical workstation. EIS was carried out on the Autolab Electrochemical workstation by applying perturbation amplitude of 5 mV in the frequency range between 0.1 MHz and 0.1 Hz.

Assembly and Electrochemical Assessment of the SIC Device: Before assembling the SIC device, the Co_2P/Sn@NC electrode was precycled three times at 50 mA g^{-1} in the half cell. The SICs were assembled using presodiated Co_2P/Sn@NC as the anode and PAC as the cathode. The PAC cathode was fabricated by the same method as the anode, except using an aluminum foil as the current collector and poly(vinylidene fluoride) (PVDF) as the binder. The separator and electrolyte were the same as those in the half cell. To obtain superior energy and power densities from the SIC, the mass ratios between the anode and cathode were selected to be 1:2.5, 1:3.5, and 1:4.5 and the voltage range was 0–4.0 V. The power and energy densities were calculated by the following formula

$$E = \int_{t1}^{t2} IV\mathrm{d}t = \frac{1}{2}C(V_{\max} + V_{\min})(V_{\max} - V_{\min}) = \frac{V_{\max} + V_{\min}}{2} \times \frac{I \times t}{m} \times \frac{1}{3.6} \quad (1)$$

$$P = \frac{3600 \times E}{t} \quad (2)$$

where $V_{\max}$ and $V_{\min}$ are the initial and final discharge voltages (V), I is the discharge/charge current (A), t is the discharge time (s), m is the total mass of the anode and cathode active material (g), E is the energy density (W h kg^{-1}), and P is the power density (W kg^{-1}).

Supporting Information

Supporting Information is available from the Wiley Online Library or from the author.

Acknowledgements

X.C.R. and Z.G.R. contributed equally to this work. This work was financially supported by National Natural Science Foundation of China (Nos. 51572100, 21875080, 51504171, and 61434001), Major Project of Technology Innovation of Hubei Province (2018AAA011), HUST Key Interdisciplinary Team Project (2016JCTD101), Wuhan Yellow Crane Talents Program, and City University of Hong Kong Strategic Research Grant (SRG) No. 7005105. The authors thank the Shanghai Synchrotron Radiation Facility (SSRF) BL08U, BL14B1, and BL15U1 staffs and also acknowledge the Nanodevices and Characterization Centre of WNLO-HUST and Analytical and Testing Center of HUST.

Conflict of Interest

The authors declare no conflict of interest.

Keywords

anode material, cobalt phosphide, sodium-ion capacitors, tin, yolk–shell

Received: January 10, 2019
Revised: February 7, 2019
Published online: February 27, 2019

[1] a) L. Li, Y. Zheng, S. L. Zhang, J. P. Yang, Z. P. Shao, Z. P. Guo, *Energy Environ. Sci.* **2018**, *11*, 2310; b) H. Wang, C. Zhu, D. Chao, Q. Yan, H. J. Fan, *Adv. Mater.* **2017**, *29*, 1702093.
[2] a) Q. Xia, H. Yang, M. Wang, M. Yang, Q. Guo, L. Wan, H. Xia, Y. Yu, *Adv. Energy Mater.* **2017**, *7*, 1701336; b) X. C. Ren, J. S. Wang, D. M. Zhu, Q. W. Li, W. F. Tian, L. Wang, J. B. Zhang, L. Miao, P. K. Chu, K. F. Huo, *Nano Energy* **2018**, *54*, 322; c) L. Y. Wu, P. F. Lu, R. G. Quhe, Q. Wang, C. H. Yang, P. F. Guan, K. S. Yang, *J. Mater. Chem. A* **2018**, *6*, 7933.
[3] a) P. Jezowski, O. Crosnier, E. Deunf, P. Poizot, F. Beguin, T. Brousse, *Nat. Mater.* **2018**, *17*, 167; b) S. Zhang, C. Li, X. Zhang, X. Sun, K. Wang, Y. Ma, *ACS Appl. Mater. Interfaces* **2017**, *9*, 17136.
[4] a) L. Shen, H. Lv, S. Chen, P. Kopold, P. A. van Aken, X. Wu, J. Maier, Y. Yu, *Adv. Mater.* **2017**, *29*, 1700142; b) J. H. Won, H. M. Jeong, J. K. Kang, *Adv. Energy Mater.* **2017**, *7*, 1601355.
[5] a) N. Yabuuchi, M. Kajiyama, J. Iwatate, H. Nishikawa, S. Hitomi, R. Okuyama, R. Usui, Y. Yamada, S. Komaba, *Nat. Mater.* **2012**, *11*, 512; b) H. Kim, H. Kim, Z. Ding, M. H. Lee, K. Lim, G. Yoon, K. Kang, *Adv. Energy Mater.* **2016**, *6*, 1600943; c) V. Aravindan, M. Ulaganathan, S. Madhavi, *J. Mater. Chem. A* **2016**, *4*, 7538; d) Z. Li, Y. Fang, J. Zhang, X. W. D. Lou, *Adv. Mater.* **2018**, *30*, 1800525.
[6] a) Y. E. Zhu, L. P. Yang, J. Sheng, Y. N. Chen, H. C. Gu, J. P. Wei, Z. Zhou, *Adv. Energy Mater.* **2017**, *7*, 1701222; b) T. Wei, G. Yang, C. Wang, *ACS Appl. Mater. Interfaces* **2017**, *9*, 31861; c) P. Wu, A. Zhang, L. Peng, F. Zhao, Y. Tang, Y. Zhou, G. Yu, *ACS Nano* **2018**, *12*, 759.
[7] a) K. Kravchyk, L. Protesescu, M. I. Bodnarchuk, F. Krumeich, M. Yarema, M. Walter, C. Guntlin, M. V. Kovalenko, *J. Am. Chem. Soc.* **2013**, *135*, 4199; b) I. A. Courtney, J. R. Dahn, *J. Electrochem. Soc.* **1997**, *144*, 2045.
[8] a) J. Y. Liao, A. Manthiram, *Adv. Energy Mater.* **2014**, *4*, 1400403; b) Y. Lee, H. Lim, S. O. Kim, H. S. Kim, K. J. Kim, K. Y. Lee, W. Choi, *J. Mater. Chem. A* **2018**, *6*, 20383.
[9] a) H. W. Zhang, X. D. Huang, O. Noonan, L. Zhou, C. Z. Yu, *Adv. Funct. Mater.* **2017**, *27*, 1606023; b) Z. Y. Wang, Z. C. Wang, W. T. Liu, W. Xiao, X. W. Lou, *Energy Environ. Sci.* **2013**, *6*, 87; c) X. S. Zhou, L. Yu, X. Y. Yu, X. W. Lou, *Adv. Energy Mater.* **2016**, *6*, 1601177.
[10] Y. S. Choi, Y. W. Byeon, J. P. Ahn, J. C. Lee, *Nano Lett.* **2017**, *17*, 679.

[11] Z. Chen, P. C. Hsu, J. Lopez, Y. Z. Li, J. W. F. To, N. Liu, C. Wang, S. C. Andrews, J. Liu, Y. Cui, Z. N. Bao, *Nat. Energy* **2016**, *1*, 15009.
[12] Z. Wang, Z. Wang, H. Wu, X. W. Lou, *Sci. Rep.* **2013**, *3*, 1391.
[13] a) L. D. Ellis, T. D. Hatchard, M. N. Obrovac, *J. Electrochem. Soc.* **2012**, *159*, A1801; b) S. Wang, Y. Fang, X. Wang, X. W. D. Lou, *Angew. Chem., Int. Ed.* **2019**, *58*, 760.
[14] L. Baggetto, H.-Y. Hah, J.-C. Jumas, C. E. Johnson, J. A. Johnson, J. K. Keum, C. A. Bridges, G. M. Veith, *J. Power Sources* **2014**, *267*, 329.
[15] Y. Kim, Y. Kim, A. Choi, S. Woo, D. Mok, N. S. Choi, Y. S. Jung, J. H. Ryu, S. M. Oh, K. T. Lee, *Adv. Mater.* **2014**, *26*, 4139.
[16] a) E. Uchaker, Y. Z. Zheng, S. Li, S. L. Candelaria, S. Hu, G. Z. Cao, *J. Mater. Chem. A* **2014**, *2*, 18208; b) L. Fan, X. Li, B. Yan, J. Feng, D. Xiong, D. Li, L. Gu, Y. Wen, S. Lawes, X. Sun, *Adv. Energy Mater.* **2016**, *6*, 1502057.
[17] B. Tian, J. Światowska, V. Maurice, C. Pereira-Nabais, A. Seyeux, P. Marcus, *J. Phys. Chem. C* **2015**, *119*, 919.
[18] Z. Le, F. Liu, P. Nie, X. Li, X. Liu, Z. Bian, G. Chen, H. B. Wu, Y. Lu, *ACS Nano* **2017**, *11*, 2952.
[19] R. Ding, L. Qi, H. Wang, *Electrochim. Acta* **2013**, *114*, 726.
[20] Z. Chen, V. Augustyn, X. Jia, Q. Xiao, B. Dunn, Y. Lu, *ACS Nano* **2012**, *6*, 4319.

ADVANCED ENERGY MATERIALS

Supporting Information

for ***Adv. Energy Mater.,*** DOI: 10.1002/aenm.201900091

Tailored Plum Pudding-Like Co_2P/Sn Encapsulated with Carbon Nanobox Shell as Superior Anode Materials for High-Performance Sodium-Ion Capacitors

Xiaochuan Ren, Zhiguo Ren, Qingwei Li, Wen Wen, Xiaofang Li, Ye Chen, Lei Xie, Liao Zhang, Daming Zhu,* Biao Gao, Paul K. Chu, and Kaifu Huo*

Supporting Information

Tailored Plum Pudding-Like Co_2P/Sn Encapsulated with Carbon Nanobox Shell as Superior Anode Materials for High-Performance Sodium-Ion Capacitors

Xiaochuan Ren[+], Zhiguo Ren[+], Qingwei Li, Wen Wen, Xiaofang Li, Ye Chen, Lei Xie, Liao Zhang, Daming Zhu, Biao Gao, Paul K. Chu, and Kaifu Huo**

X. C. Ren, Z. G. Ren, Q. W. Li, X. F. Li, Y. Chen, L. Xie, L. Zhang, Prof. K. F. Huo
Wuhan National Laboratory for Optoelectronics (WNLO), Huazhong University of Science and Technology, Luoyu Road 1037, Wuhan 430074, China
Email: kfhuo@hust.edu.cn (K. F. Huo)

Dr. W. Wen, Dr. D. M. Zhu
Shanghai Synchrotron Radiation Facility, Shanghai Advanced Research Institute, Chinese Academy of Sciences, Shanghai 201204, China
Email: zhudaming@sinap.ac.cn (D. M. Zhu)

Dr. B. Gao
The State Key Laboratory of Refractories and Metallurgy, Institute of Advanced Materials and Nanotechnology, Wuhan University of Science and Technology, Wuhan 430081, China.

Dr. B. Gao, Prof. P. K. Chu
Department of Physics and Department of Materials Science and Engineering, City University of Hong Kong, Tat Chee Avenue, Kowloon, Hong Kong, China

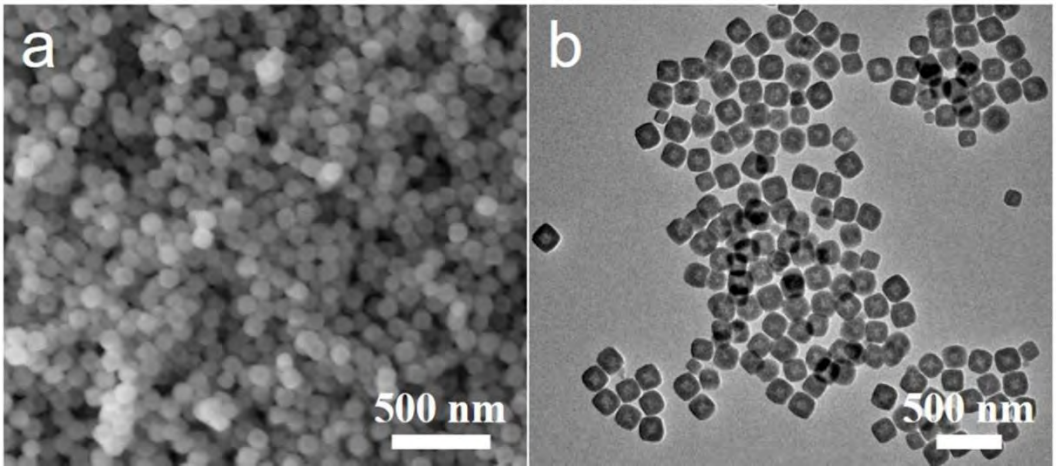

Figure S1. SEM (a) and TEM (b) images of $CoSn(OH)_6$ nanocubes.

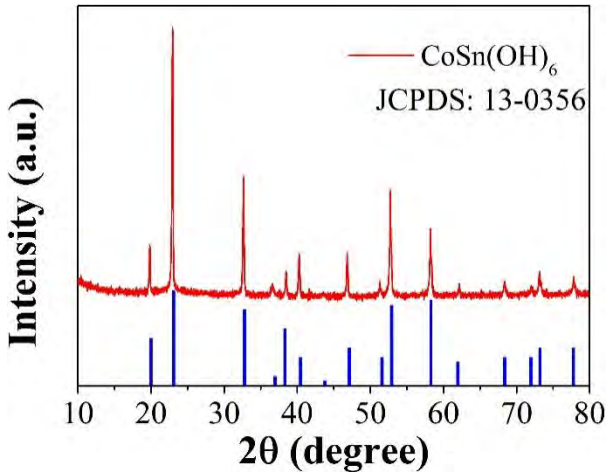

Figure S2. XRD pattern of $CoSn(OH)_6$ nanocubes.

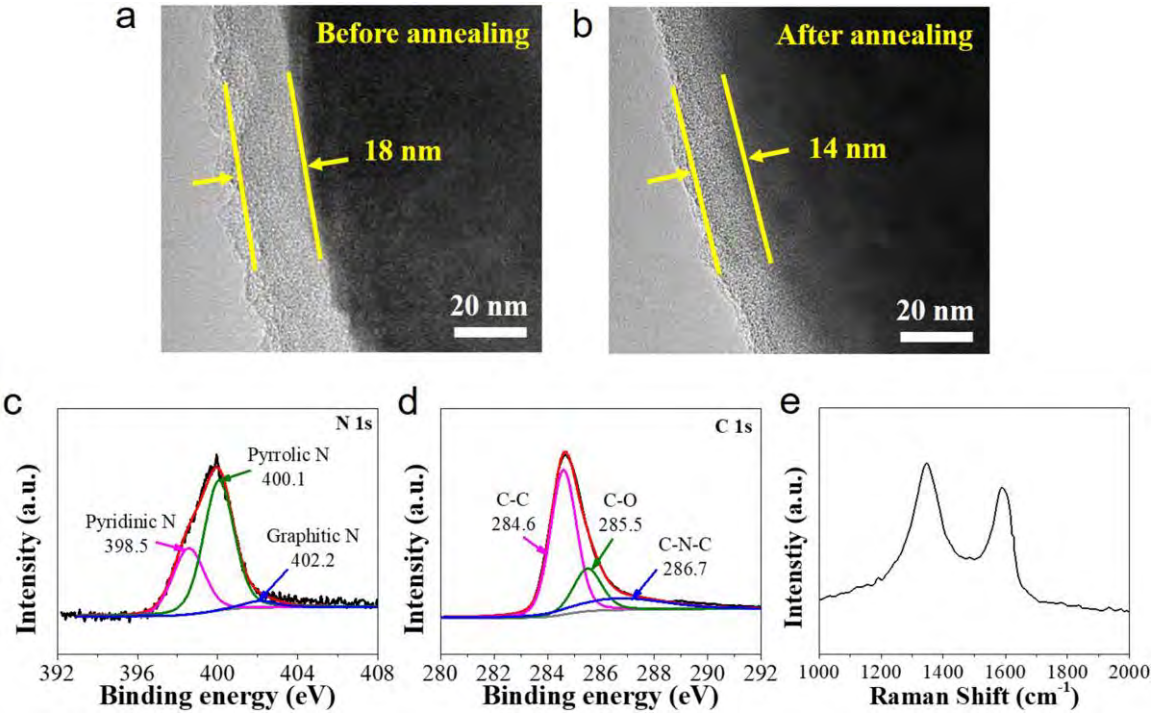

Figure S3. TEM images of $CoSn(OH)_6$@PDA before (a) and after (b) annealing. High-resolution XPS spectra of N1s (c), C 1s (d) and Raman spectrum (e) of Co_2P/Sn@NC.

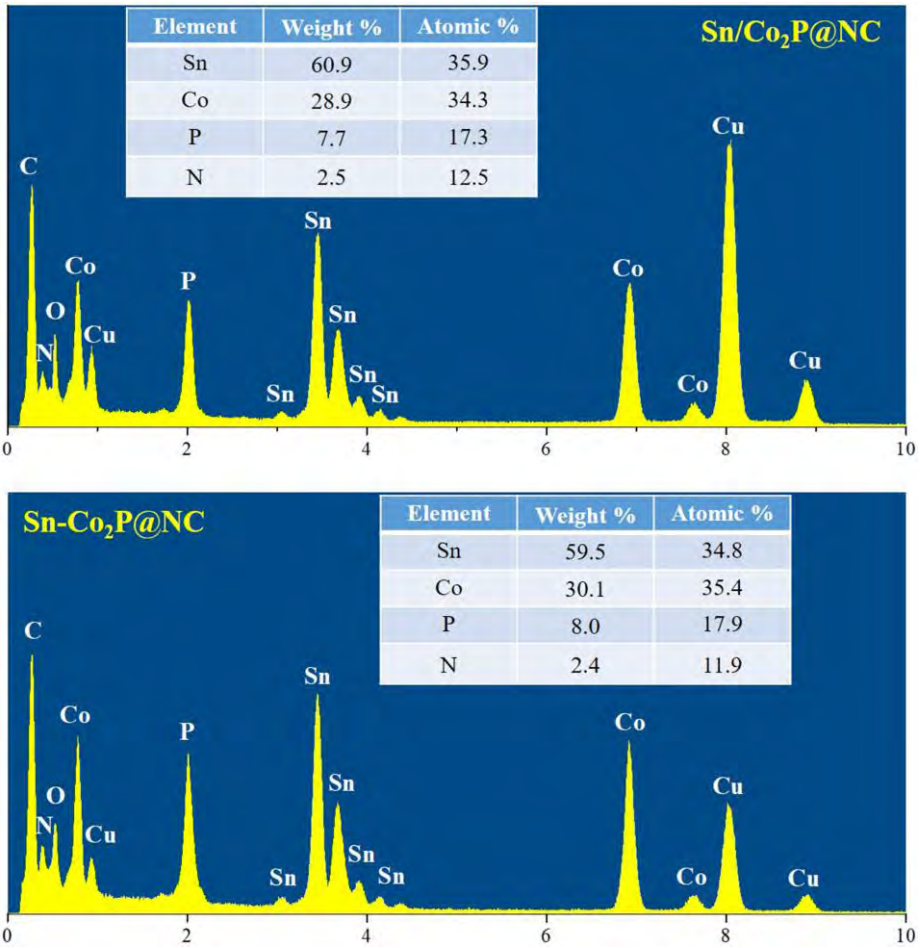

Figure S4. EDS pattern of the Co_2P/Sn@NC and Co_2P-Sn@NC nanobox.

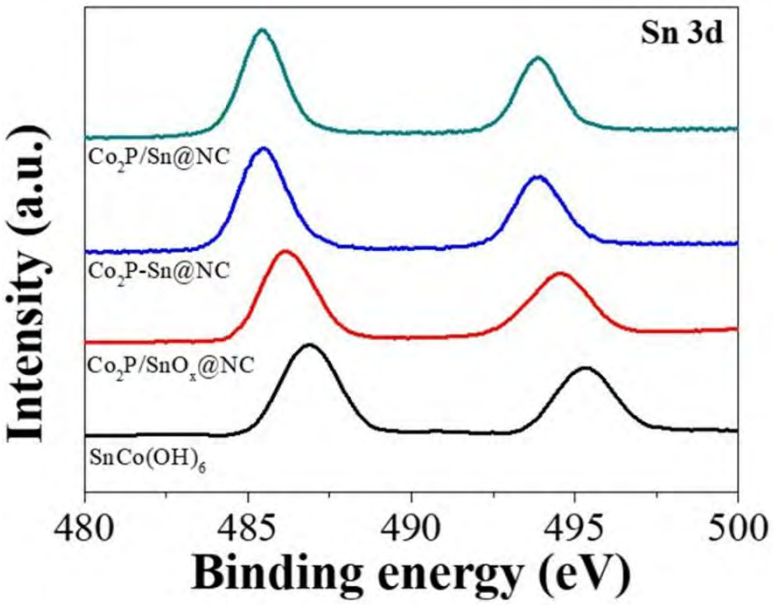

Figure S5. The Sn 3d XPS spectra of Co_2P/Sn@NC and Co_2P-Sn@NC, Co_2P/SnO_x@NC and $CoSn(OH)_6$**.**

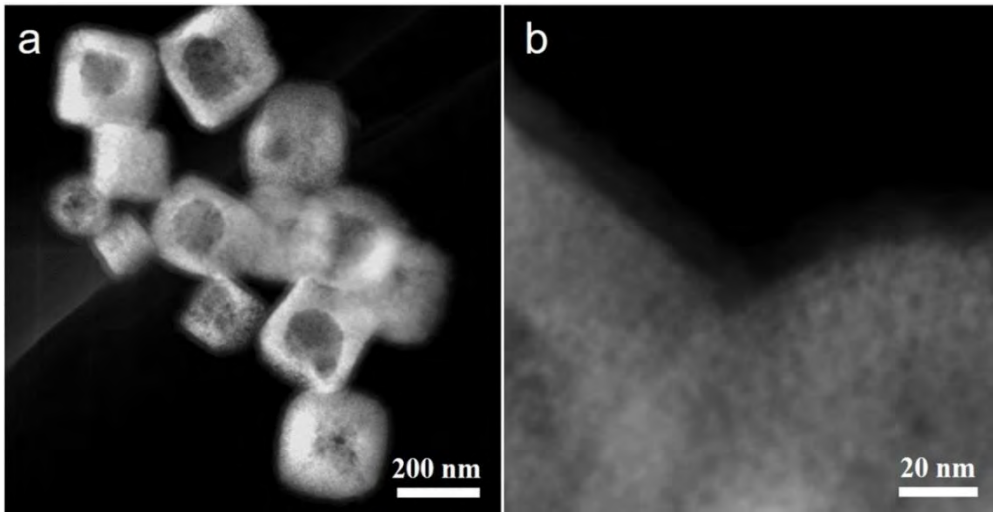

Figure S6. HAADF-STEM images of Co_2P/Sn@NC.

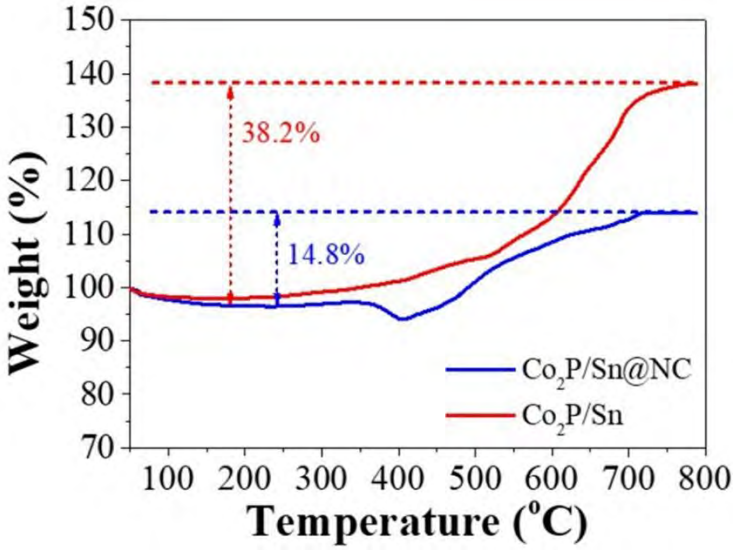

Figure S7. TGA curves of Co_2P/Sn@NC and as-prepared Co_2P/Sn without carbon shell.

Thermogravimetric analysis (TGA) is used to estimate the content of carbon in Co_2P/Sn@NC. In both cases, the TGA curves show a weight loss before 250 ^oC that corresponds to the loss of the adsorbed water. The TGA profile of Co_2P/Sn displays an obvious weight increase in the range of 250 to 800 ^oC due to the gradual oxidation of Sn to SnO_2 and Co_2P to Co_3O_4 and P_2O_5. In comparison, the lower weight gain of Co_2P/Sn@NC is attributed to the burning of the carbon component. Therefore, the content of carbon in Co_2P/Sn@NC is calculated to be 23.4 wt%.

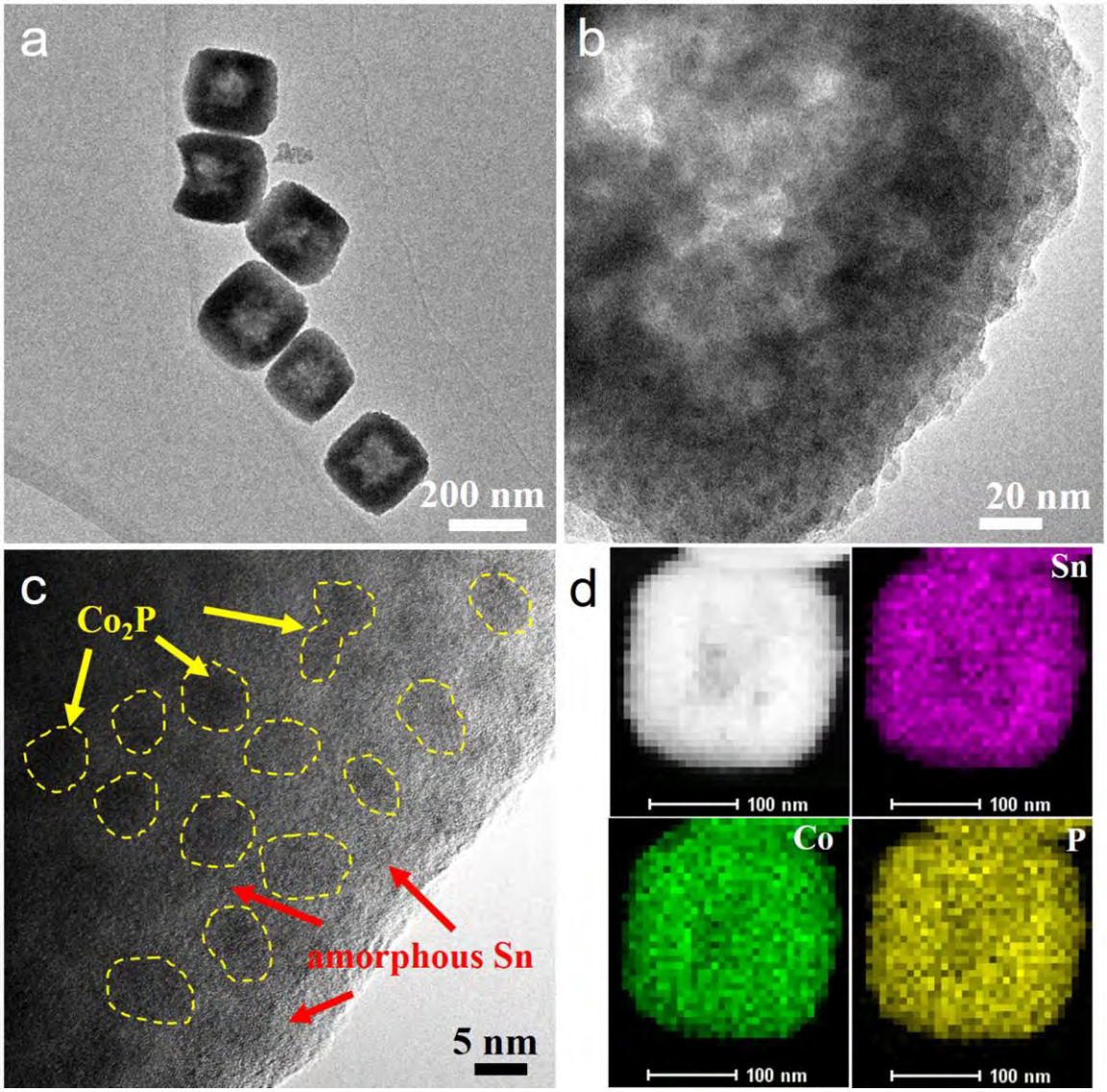

Figure S8. TEM (a, b) and HRTEM (c) images of Co_2P/Sn nanoboxes without the coating of carbon shell. (d) The elemental maps of Co_2P/Sn.

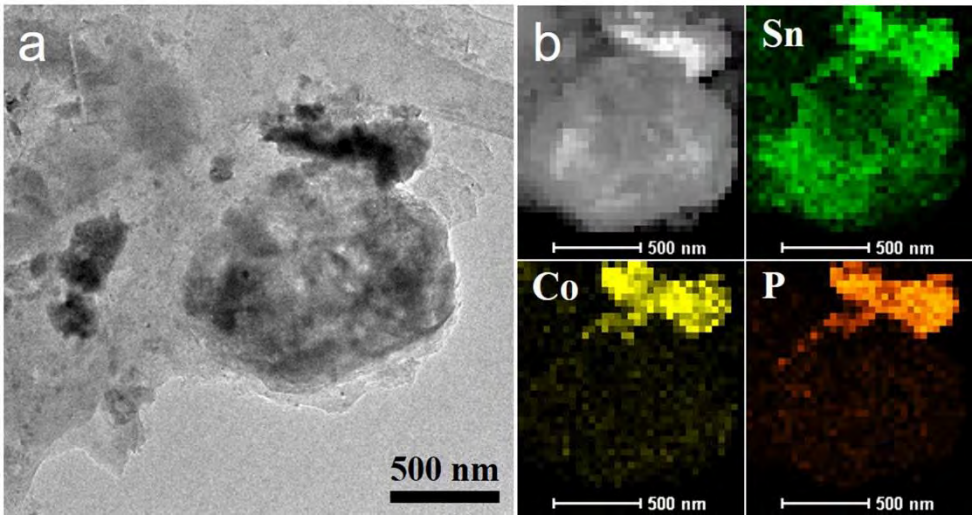

Figure S9. (a) The TEM image and (b) the corresponding elemental maps of Co_2P-Sn without the coating of carbon shell.

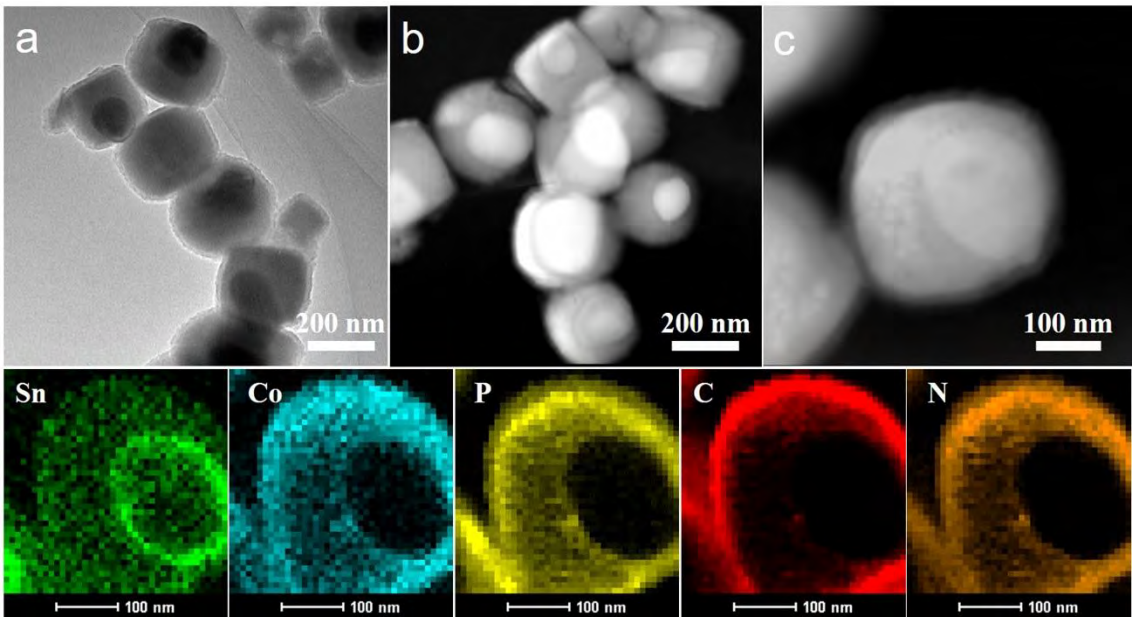

Figure S10. (a) The TEM image, (b, c) HAADF-STEM images and corresponding elemental maps of Co_2P-Sn@NC.

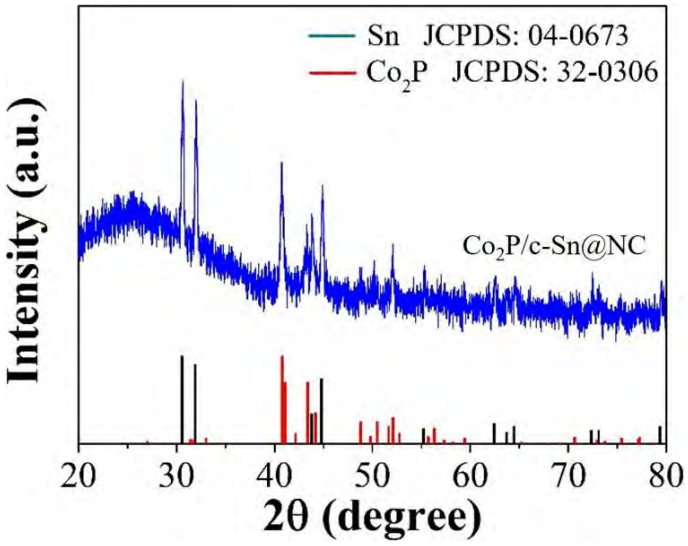

Figure S11. XRD pattern of the Co_2P-Sn@NC nanoboxes.

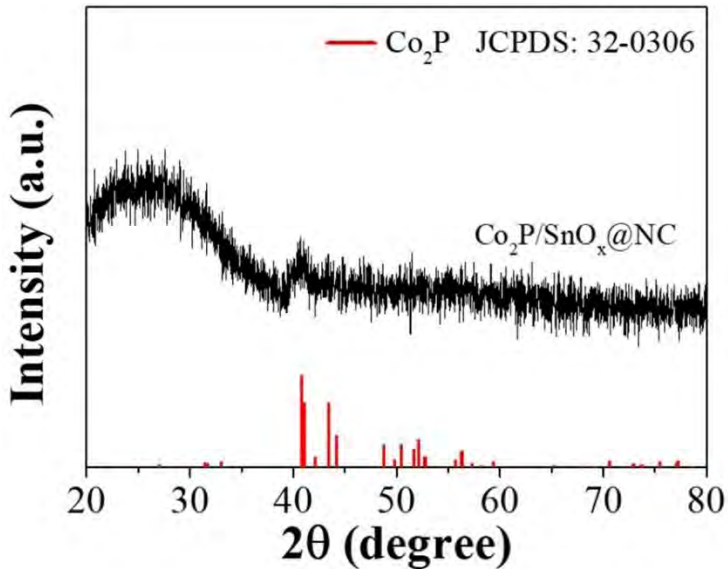

Figure S12. XRD pattern of Co_2P/SnO_x@NC.

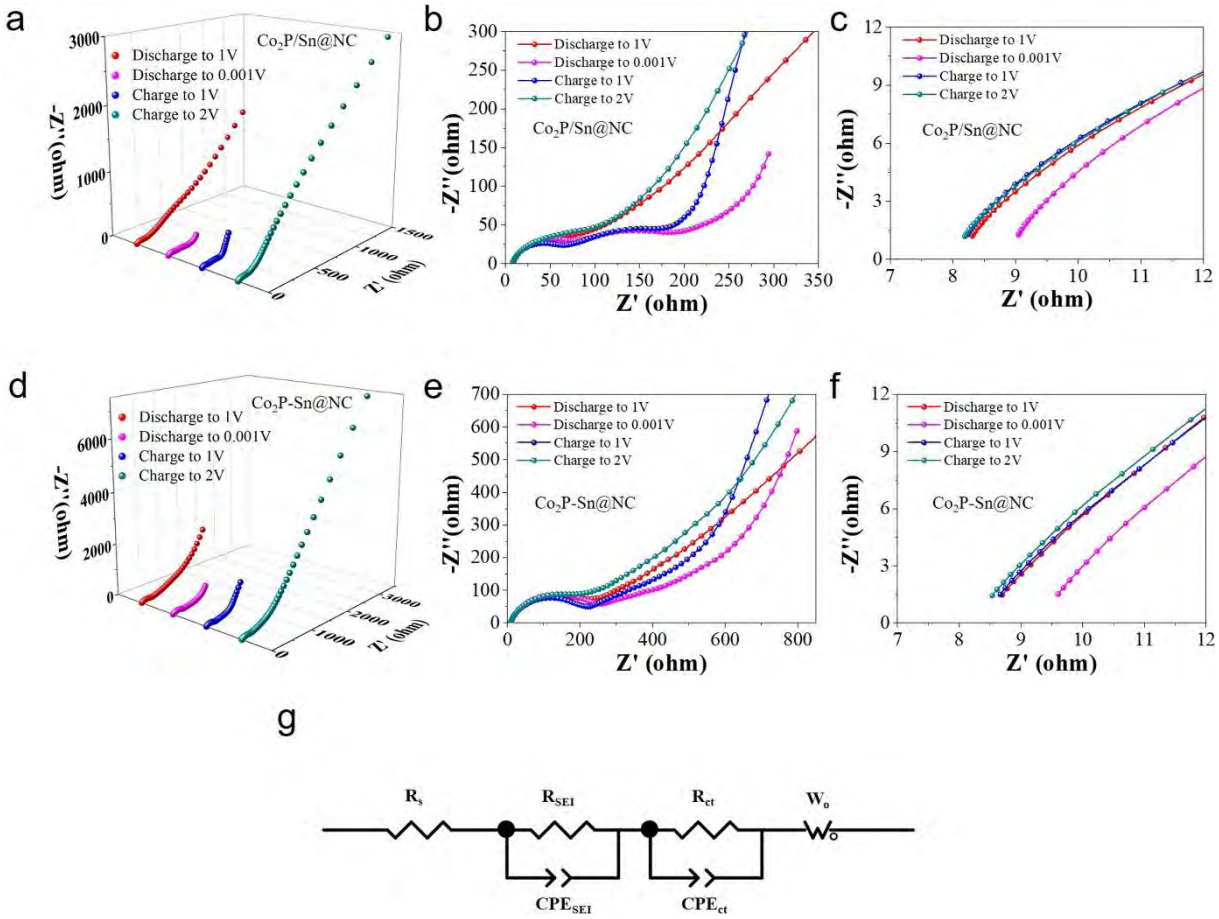

Figure S13. EIS measurements of the (a-c) Co_2P/Sn@NC and (d-f) Co_2P-Sn@NC electrodes at various charge/discharge stages. (g) The equivalent circuit used for EIS fitting (R_s: Ohmic resistance including electrolyte and contact resistance; R_{SEI}: SEI film resistance; R_{ct}: charge transfer resistance; W_o: Warburg impedance; CPE_{SEI} and CPE_{ct}: constant phase element)

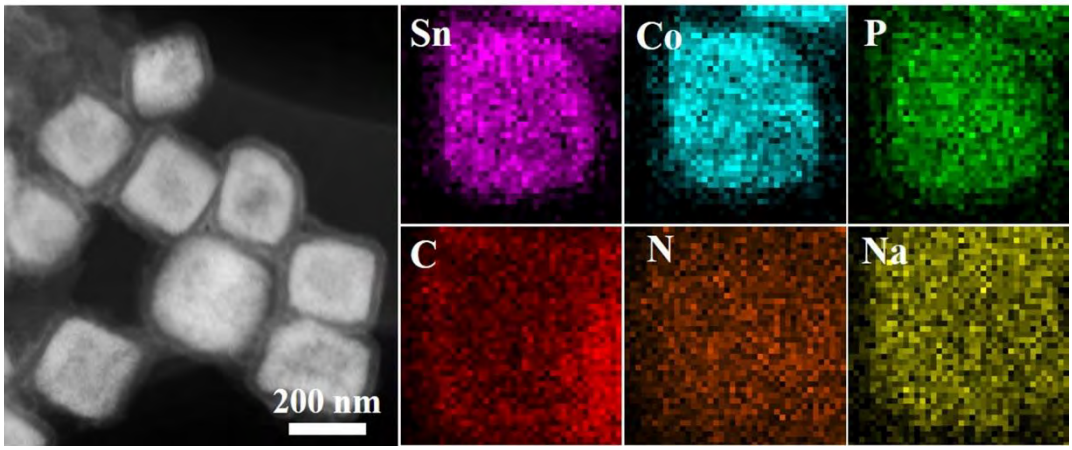

Figure S14. (a) HAADF-STEM image and (b) corresponding EDS mapping of Co_2P/Sn@NC at the discharged state of 0.001 V.

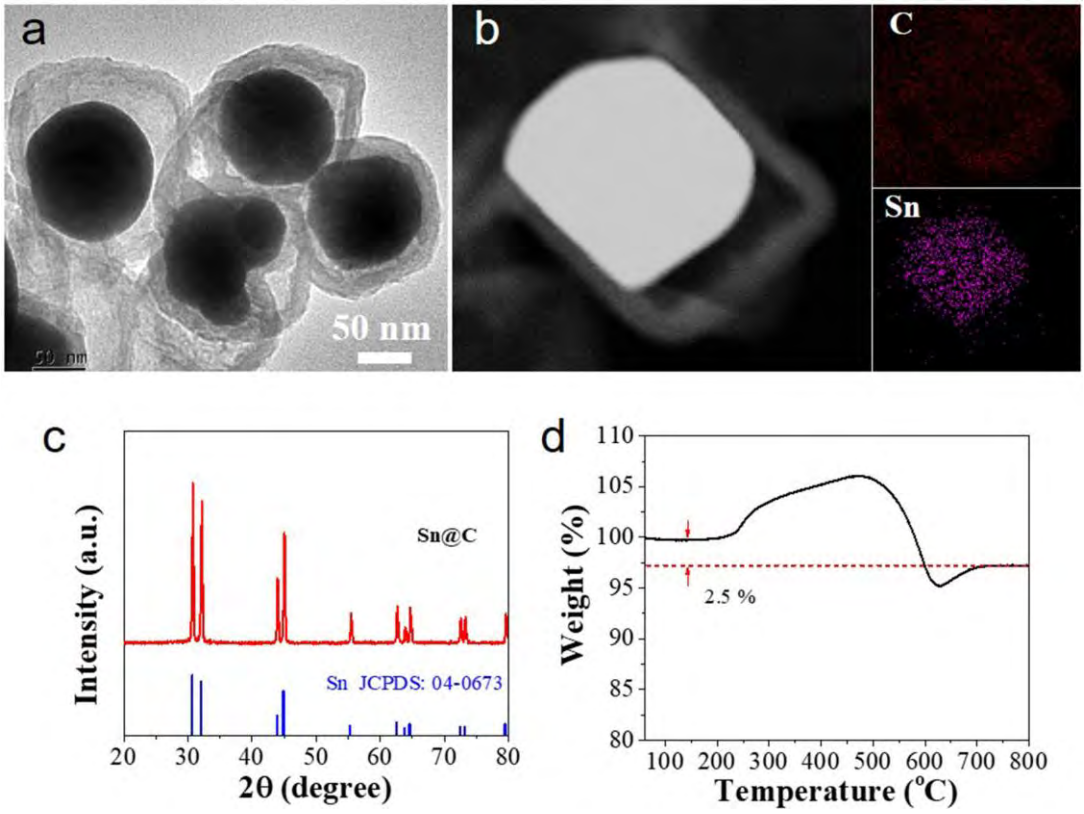

Figure S15. (a) TEM image, (b) HAADF-STEM image and corresponding elemental maps, (c) XRD pattern and (d) TGA profile of Sn@C nanobox.

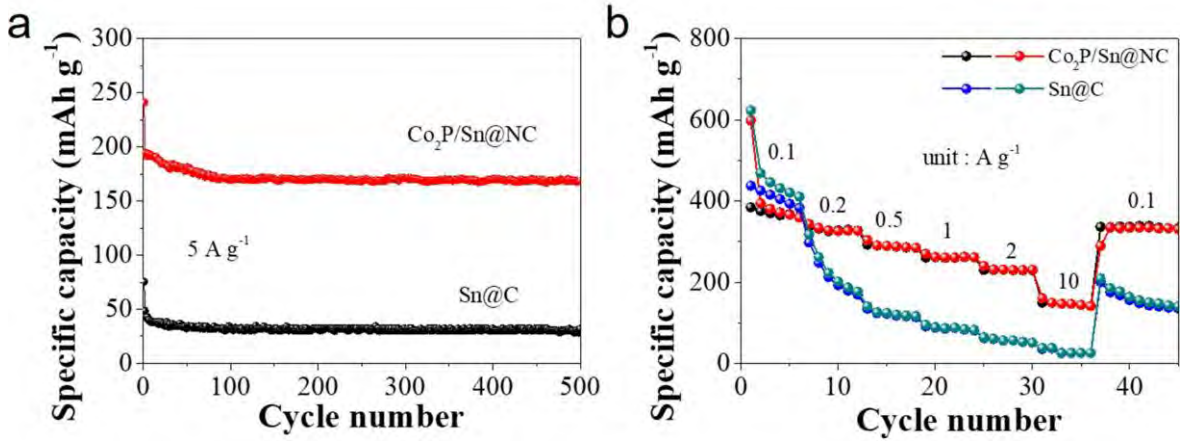

Figure S16. (a) Cycling performances and (b) rate capability of Sn@C and Co_2P/Sn@NC electrodes.

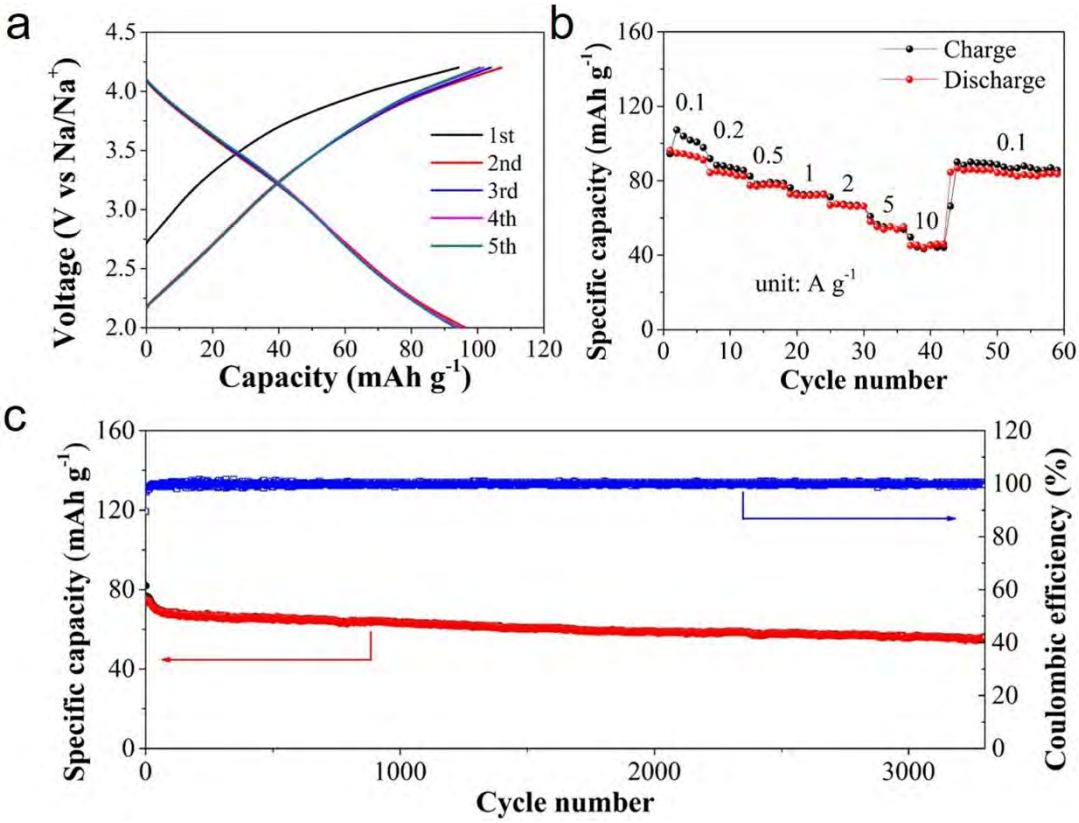

Figure S17. (a) The typical charge/discharge curves of PAC between 2.0-4.2 V at 0.1 A g^{-1}. (b) The rate capability and (c) cycling performance with coulombic efficiency after 3300 cycles at a current density of 1.0 A g^{-1}.

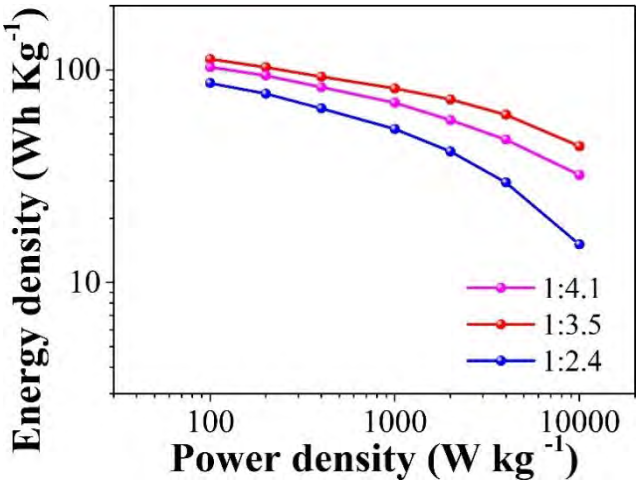

Figure S18. Ragone plots of Co_2P/Sn@NC//PAC SIC devices with different mass ratios of anode and cathode materials in the voltage range of 0 - 4.0 V.

Table S1. The Warburg impedance coefficient (σ_w) and diffusion coefficient of Na^+ (D_{Na}) of the Co_2P/Sn@NC and Co_2P-Sn@NC electrodes.

Potential	**Co_2P/Sn@NC**		**Co_2P-Sn@NC**	
	σ_w (Ω $s^{-1/2}$)	**D_{Na} (cm^2 s^{-1})**	**σ_w (Ω $s^{-1/2}$)**	**D_{Na} (cm^2 s^{-1})**
Discharge to 1.0 V	257.8	2.4×10^{-16}	254.5	2.5×10^{-16}
Discharge to 0.001 V	23.0	8.2×10^{-16}	82.0	6.4×10^{-17}
Charge to 1.0 V	26.3	2.3×10^{-14}	111.1	1.3×10^{-15}
Charge to 2.0 V	59.1	5.7×10^{-15}	869.4	2.7×10^{-15}

Table S2. Electrochemical performance comparisons of the Co_2P/Sn@NC electrode with the reported Sn-based anodes for SIBs.

Electrodes	Current density (mA g^{-1})	Cycle number/ fading rate per cycle (cycles/%)	Capacity at various rates (mAh g^{-1} at A g^{-1}) Based on total mass	Capacity at various rates (mAh g^{-1} at A g^{-1}) Based on Sn mass	Ref.
$Fe_{0.74}Sn_5$@RGO	50	80/0.8	200 at 0.5		1
Hollow Sn	50	35/1.1		142 at 0.4	2
Sn/SnO_2/C	20	200/0.38	120 at 1		3
G/Sn@C	100	-	166 at 1.6 106 at 3.2		4
Sn@N-C	100	150/0.45	177 at 1 117.1 at 2		5
Sn nanodots/NC	50	300/0.08	205 at 2 149 at 5		6
$FeSn_2$-C	100	100/0.19	200 at 1		7
SnCu	50	100/0.6	207 at 0.2		8
Sn/ordered C	100	200/0.09	228 at 1		9
Sn@NCNFs	84.7	450/0.03		400 at 0.846 290 at 1.692 190 at 4.23	10
Sn/Co@C	100	120/0.11	228 at 1		11
SnSb/NC	100	200/0.1	95 at 2		12
Sn nanodendrites	100	300/0.01		430 at 2.583 370 at 4.23	13
Self-healing Sn	8760	5000/0.000036		619 at 6.768 299 at 13.53	14
SnO_x-Sn	100	250/0.07	390 at 0.5 338 at 1		15
$Sn_2P_2O_7$/RGO	2000	15000/0.0025	250 at 2 170 at 10		16
Sn/Co_2P@NC	**5000**	**10000/0.0012**	**394 at 0.1 264 at 1 233 at 2 147 at 10**	**566 at 1 500 at 2 394 at 5 315 at 10**	**this work**

References

[1] F. X. Xin, H. J. Tian, X. L. Wang, W. Xu, W. G. Zheng, W. Q. Han, *ACS Appl. Mater. Interfaces* **2015**, *7*, 7912.

[2] Y. Y. Cheng, J. F. Huang, R. Z. Li, Z. W. Xu, L. Y. Cao, H. B. Ouyang, J. Y. Li, H. Qi, C. W. Wang, *Electrochim. Acta* **2015**, *180*, 227.

[3] Y. Y. Cheng, J. F. Huang, J. Y. Li, Z. W. Xu, L. Y. Cao, H. Qi, *J. Power Sources* **2016**, *324*, 447.

[4] B. Luo, T. F. Qiu, D. L. Ye, L. Z. Wang, L. J. Zhi, *Nano Energy* **2016**, *22*, 232.

[5] B. Ruan, H. P. Guo, Y. Hou, Q. Liu, Y. Deng, G. Chen, S. L. Chou, H. K. Liu, J. Z. Wang, *ACS Appl. Mater. Interfaces* **2017**, *9*, 37682.

[6] H. J. Ying, S. L. Zhang, Z. Meng, Z. X. Sun, W. Q. Han, *J. Mater. Chem. A* **2017**, *5*, 8334.

[7] E. Edison, R. Satish, W. C. Ling, N. Bucher, V. Aravindan, S. Madhavi, *J. Power Sources* **2017**, *343*, 296.

[8] R. E. Zhang, Z. F. Wang, W. Q. Ma, W. Yu, S. S. Lu, X. Z. Liu, *RSC Adv.* **2017**, *7*, 29458.

[9] L. Luo, H. Qiao, W. Z. Xu, D. W. Li, J. D. Zhu, C. Chen, Y. Lu, P. Zhu, X. W. Zhang, Q. F. Wei, *J. Solid State Electr.* **2017**, *21*, 1385.

[10] M. Sha, H. Zhang, Y. T. Nie, K. Q. Nie, X. X. Lv, N. Sun, X. K. Xie, Y. Y. Ma, X. H. Sun, *J. Mater. Chem. A* **2017**, *5*, 6277.

[11] B. Huang, J. W. Yang, Y. W. Li, S. H. Xiao, Q. Q. Chen, *Mater. Lett.* **2018**, *210*, 321.

[12] D. H. Youn, H. Park, K. E. Loeffler, J.-H. Kim, A. Heller, C. B. Mullins, *ChemElectroChem* **2018**, *5*, 391.

[13] C. Kim, I. Kim, H. Kim, M. K. Sadan, H. Yeo, G. Cho, J. Ahn, J. Ahn, H. Ahn, *J. Mater. Chem. A* **2018**, 6, 22809.

[14] M. Sha, H. Zhang, Y. Nie, K. Nie, X. Lv, N. Sun, X. Xie, Y. Ma, X. Sun, *J. Mater. Chem. A* **2017**, *5*, 6277.

[15] D. Cheng, J. Liu, X. Li, R. Hu, M. Zeng, L. Yang, M. Zhu, *J. Power Sources* **2017**, *350*, 1.

[16] X. Yang, R. Y. Zhang, J. Zhao, Z. X. Wei, D. X. Wang, X. F. Bie, Y. Gao, J. Wang, F. Du, G. Chen, *Adv. Energy Mater.* **2018**, *8*, 1701827.